國立臺灣大學電機資訊學院電信工程學研究所

碩士論文

Graduate Institute of Communication Engineering

College of Electrical Engineering and Computer Science

National Taiwan University

Master Thesis

使用 CVF 與新創輪廓擷取演算法於自動心臟磁振影像左心室分割

Automated Left Ventricle Segmentation in Cardiac Short-Axis MR Images Using
Cost-Volume Filtering and Novel Myocardial Contour Processing Framework
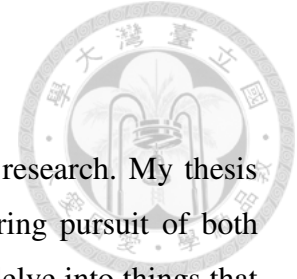
張安政

An-Cheng Chang

指導教授：鄭士康 博士

Advisor: Shyh-Kang Jeng, Ph.D.

中華民國 103 年 10 月

October, 2014

ACKNOWLEDGEMENTS

I feel tremendously lucky to be given complete freedom over my research. My thesis advisor and mentor, Dr Shyh-Kang Jeng, showed me his unwavering pursuit of both knowledge and wisdom. His student-first philosophy allows me to delve into things that I am passionate of. I could not have asked for a finer teacher than him.

I would like to express my gratitude to Dr Soo-Chang Pei, Dr Hsiao-Wen Chung, Dr Jian-Jiun Ding, and Dr Teng-Yi Huang for agreeing to serve on my oral committee and providing me with fruitful feedbacks. Their opinions on my research make this master's thesis more complete.

I want to thank my friends in the grad school and the lab. Charles is one of the most energetic person I have seen, and we have been through lots of challenging but rewarding activities thanks to him being my best partner and supporter. Hugo, Leon, and Danny— together we went to the gym in the after-hours and in the early mornings, and instilled in each other the "work hard and play hard" mantra. Thanks Lammin and Pei for taking their time joining me at lunches and dinners, even though they were sometimes pretty much fully occupied trying to meet deadlines. I also want to thank the peers and seniors in the lab who had helpful discussions with me that would ultimately contribute to my successful thesis defense. And my gratitude to Dafei and Kenny, who helped me with publishing the paper.

Additional thanks go to the university faculties and staffs who dedicated themselves to make IAC Workshop happen. Really sad to hear that the Ministry of Education discontinued to fund this program, because as a participant, I had one of the best teamwork experiences, best English classes, and the best lunchboxes all wrapped into one. Thanks to our German study group members Tracy, Tim, and Alice, where we once learned to sing *O Tannanbaum* on Christmas Eve, and my German teachers Michael, Christian, and Chris. They made my life as a graduate student so much more enjoyable. I want to thank those who gave me strength, especially to Karen, who has been an unfailing source of support and inspiration for me during my most difficult times. I am thankful to everyone who has encouraged and believed in me.

Last but not least, all of this would not be possible without the support of my family throughout the years. And this is dedicated to them.

摘要

　　心血管疾病通常伴隨異常的心臟功能參數，舉凡過高或過低的左心室射出分率（ejection fraction）、心輸出量（cardiac output）的不足等。這些心臟功能參數可以從心臟磁振影像（CMR images）的掃描結果加以處理推估而得，其中重要環節即為影像分割技術。過去的自動左心室影像分割演算法的效能通常受限於複雜的心肌內壁結構，或者較為繁複的使用者操作。鑑此，本研究提出自動化的高精確度心臟磁振影像左心室分割演算法。為了克服磁振造影失真現象與心肌內壁不規則結構—如心肉柱及乳狀肌—所造成的影像分割難度，其結合了針對心臟磁振影像調校的 cost-volume filtering 技術與新創的心肌輪廓擷取演算法以達到此目的。實驗結果顯示切割精準度和可靠性皆優於先前方法，並因此減少校正所需時間，自動導出的心臟功能參數與人工計算結果則呈高度相關性。各項數據顯示本研究所提出的心臟磁振影像左心室分割演算法是現今效能最好的演算法之一。

ABSTRACT

Cardiovascular diseases are often associated with abnormal **left ventricular (LV)** cardiac parameters, such as deviation of ejection fraction (EF) and cardiac output. These information can be extracted from **cardiac magnetic resonance (CMR)** scans of the heart, which involves image segmentation in CMR images. Previous works on left ventricle segmentation in CMR images are often hindered by complex inner heart wall geometry or they require a more involved operator intervention. In this work, we employ novel **cost-volume filtering (CVF)** scheme combined with novel myocardial contour processing framework to overcome the segmentation difficulty resulted from MR imaging artifacts and inner heart wall irregularities (e.g., papillary muscle and trabeculae carneae). Result shows improved accuracy and robustness over previous works. In clinical aspects, quantitative analysis shows close agreement between manually and automatically determined cardiac functions with no systematic bias in EF estimation error.

CONTENTS

LIST OF FIGURES

LIST OF TABLES

Chapter 1   Introduction

1.1   Motivation

Cardiovascular disease (CVD), an umbrella term for a myriad of conditions affecting the heart and the blood vessels, is the top-occurring disease in many places in the world. In 2008 alone, this deadly disease claimed an estimated 17.3 million lives, according to the World Health Organization, making it the single largest cause of death worldwide [1]. Aside from high mortality rate, the prevalence of CVD continuously imposes a heavy burden on the economy and public healthcare system of those affected countries. In fact, coronary heart disease, one common type of CVD, costs the United States as much as $108.9 billion each year [2]. Experts and specialists thus call for a constant effort to reduce mortality rate and the cost involved through proper prevention, identification, and monitoring following the diagnosis of the disease. While recent decades have seen a decrease of mortality rate of CVD in industrialized countries, its surge in the developing countries makes CVD remain the deadliest disease in the world [3].

Diagnosing subject's cardiac health in the early stages is therefore a key step to facilitate further treatments and increase the chance of survival, which requires, among others, quantitative assessment of the cardiac health. These include measuring myocardial mass (MM), peak ejection rate (PER), peak filling rate (PFR), ejection fraction (EF), stroke volume (SV) and its associated cardiac output (Q). In particular, cardiovascular diseases are often related with deviation of cardiac output Q, derived from segmenting left ventricle (LV) in cardiac magnetic resonance (MR) images over a cardiac cycle.

As the cardiac cine MR scan of one patient consists of a few dozen to several hundred individual images to work on, segmenting the ventricle by trained operator consumes a considerable amount of time and manpower. Another drawback of manual segmentation
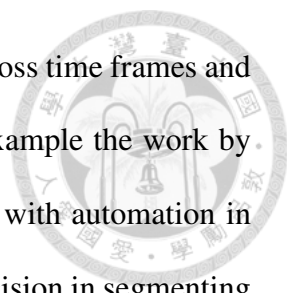
is that it is prone to operator bias due to complex inner myocardial structures such as the papillary muscles and trabeculae carneae [4]. Therefore, automation of this task highly appeals to clinicians as it is able to eliminate such operator bias and expedite the evaluation process. At this moment, however, the popular commercial software MASS provides merely moderately usable segmentation results and the resulting cardiac parameters are less reliable [5], which would require more operator intervention to correct failed segmentations. Nevertheless, because of its popularity and ability of full integration into MRI scanning workflow, it has been compared against as a baseline algorithm by many previous works [4], [6].

Segmenting the ventricles in cardiac magnetic resonance (CMR) images by automation is not trivial, even in noiseless cases. Challenges are: 1) substantial shape variation across slices and timeframes, 2) inter-subject variation resulted from different pathologies, and 3) various distortions of the MR image itself, such as partial volume effect, field inhomogeneity, and low contrast between myocardium and lungs. Moreover, many previous works did not achieve full automation; some require a training set prior to segmentation, others require a coarse contour as initialization. Despite ongoing research on the CMR image segmentation, it is still acknowledged as an open problem by a recent survey [7].

1.2   Research Goal

As there are many previous works on automation of left ventricle segmentation that still require some degree of human intervention before and during the segmentation process (such as constructing training sets and priors, which we will point out in Section 1.4), we therefore look to lessen the those restrictions and aiming for maximum automation.

Despite many previous methods attempting to ensure consistency across time frames and slices of the CMR 4D volume, there are however only a few, for example the work by Lee *et al.* and Jolly *et al.*, that attempt to provide a robust solution with automation in mind. Therefore, this thesis dedicates the goal to automation and precision in segmenting left ventricle in cardiac cine MR images. The main objectives are:

- Full automation: it requires no manual intervention before and during the segmentation process.

- Precise segmentation: despite aiming for full automation, the segmentation precision is not to be sacrificed. More so, the result must be up to par with the state-of-the-art in order to have a meaningful impact in this field.

- Eliminate operator bias: by providing robust, reliable segmentation algorithm for clinical use, intra- and inter-observer variability are resulted from hand-drawing left ventricle myocardium contours can be eliminated

- Estimate crucial cardiac parameters: these parameters are indispensable in assessing cardiac functions of the patient, including ejection fraction, peak ejection rate, etc.

For the purpose of maximum automation, we have developed an image-driven approach. The operator is not required to construct any prior model or trace left ventricle contour in order to initialize the algorithm. We argue that a general prior model is insufficient to describe all possible cases which often leads to inaccurate segmentation, shows the literature survey. In fact, we believe minimal assumption is the key to the proposed method's superiority and robustness against various pathologies.
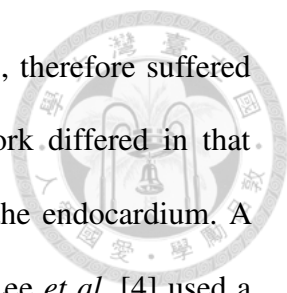
1.3 Contribution

We have employed novel cost initialization scheme for the cost-volume-filtering (CVF) based image segmentation. Together with novel myocardial contour processing framework, the proposed computational framework is able to overcome the segmentation difficulty caused by PMTC (papillary muscle and trabeculae carneae) tissues that prevent previous methods from achieving high segmentation accuracy.

1.4 Literature Survey

Segmentation of cardiac magnetic resonance (CMR) images has been an area of active research for the past two decades; it has accumulated a considerable amount of work so far. For starters, Petitjean *et al.* [7] compiled a comprehensive list of recent works up until 2011, which is a good introduction for newcomers in this field. In this section, we limit our scope of the literature survey and focus on the segmentation of the left ventricle (LV) in short-axis view MR images.
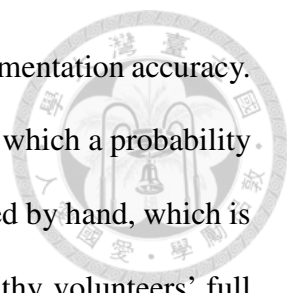
A class of approach using region- or edge-based methods often involves the use of binary thresholding, region growing, and edge-detection, and mathematical morphology [4], [8]–[14]. Lu *et al.* [11] identifies the LV cavity among candidates according to the roundness metric of each connected component. Then, for extracting the LV endocardium, Otsu's optimal thresholding [15] and convex hull fitting are applied to the selected LV cavity. As for the epicardium, they use region growing and morphological operation refinements to segment the muscle wall. In the last stage of the algorithm, both contours are smoothed by taking higher frequency components out of each contour's respective Fourier descriptor. The drawback is the algorithm failed in image slices with left ventricular outflow tract (LVOT); they later extended their work to address this issue [6].

Huang *et al.* [10], [12] followed a similar processing flows as Lu's, therefore suffered from similar failure in the presence of LVOT. However, their work differed in that gradient information is taken into consideration when delineating the endocardium. A performance improvement over Lu's previous work was reported. Lee *et al.* [4] used a hybrid of region-growing and active contour driven by modified gradient field to extract endocardium and epicardium respectively, and the results show high correlation between manual and computed cardiac functions.

Another class of approach can be listed under the category called deformable models, which involves the use of active shape and appearance model (ASM/AAM) and level set methods. In principle, a shape or a contour, which usually starts from an initial contour annotated by the operator, iteratively deforms, where it's deformation is driven by both the external force (such as gradient or local intensity distribution) and internal force (such as smoothness constraint) [16]–[19]. These approaches have the additional flexibility to incorporate shape priors or motion models [20]–[23]. For instance, Lynch *et al.* [20] encoded the parametric volume-over-time model into the evolution of level set. It achieved only moderate results measured by correlation, possibly due to its emphasis on temporal constraint, thus overlooking the information from the images themselves. Schaerer *et al.* [22] also sought to incorporate motion model into the processing flow, but suffered from similar sub-par segmentation accuracy.

Aside from the flexible deformable models paradigm, many other approaches are attempted as well. Jolly [24] proposed a minimal surface approach. Candidate contours are first computed from the average of a particular slice across all time frames registered to a particular phase. Those candidate contours are transformed back to respective time frames, and finally propagated to other slices. Minimal surface is computed using these back-transformed candidate contours as boundary constraints. It is fully automatic, offers

temporal and inter-slice consistency, but comes at the price of less segmentation accuracy. Lorenzo-Valdés *et al.* [25] used probabilistic atlas-based approach in which a probability prior for each tissue class (e.g., myocardium, LV cavity) is constructed by hand, which is very laborious—they reported to have manually segmented 14 healthy volunteers' full MR 4D volume, which translates to segmenting hundreds of MR images. And given that they only train the model using healthy case, the reliability is overshadowed by unforeseen pathologies because the performance relies on the training set. On the other hand, training a wide set of models in an attempt for more accuracy seems to negate the benefit of automation in the first place.

1.5   Thesis Outline

Chapter I highlights the motivation and contribution of this study, as well as an overview of previous studies in CMR segmentation. In Chapter II, we briefly review the anatomy of the heart before guiding the reader through the cardiac MR images. In Chapter III, we introduce the proposed computational framework for segmenting the left ventricle in short-axis view cardiac cine MR images. Experimental results and as well as detailed discussions regarding the performance of proposed method are shown in Chapter IV. And finally, Chapter V marks the conclusion and future prospect of this work.

Chapter 2 Fundamentals
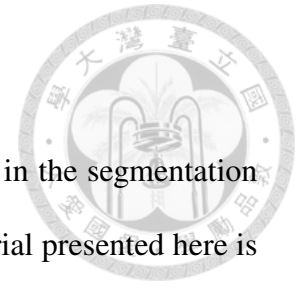
In this chapter, we establish some background knowledge involved in the segmentation of CMR images from both medical and technical aspects. The material presented here is not intended to be comprehensive. Instead, it aims at providing individuals not familiar with working with medical images the prerequisite to understand the materials presented in the ensuing chapters.

2.1 Cardiac Magnetic Resonance Imaging

Cardiac magnetic resonance (CMR) imaging is a non-invasive imaging modality for visualizing the function and structure of the cardiovascular system. Its 3D capability and high spatial resolution has allowed itself to be established as a clinical practice for treatment of the cardiovascular disease. Unlike X-ray computed tomography (CT) using ionizing radiation which can damage the cells and cause cancer, magnetic resonance imaging poses no such risk to human body and is agreed by experts to be non-hazardous [26]. CMR imaging differs from typical MR in that CMR uses electrocardiogram (ECG) gating as means of synchronization over several cardiac cycles in order to obtain a better resolved image. Real-time CMR is possible, but at the expense of lower image quality.

2.2 Ventricles in Cardiac MR Short-Axis View

The standard procedure for volumetric measurements of the ventricles is to position the scanning plane so that the plane is perpendicular to the long-axis of the heart. The imaging plane moving along the long-axis begins from just below the atrium down to the bottom of the heart, scanning the whole ventricle in order to obtain its 3D volume data. The 2D image in this acquired stack of 3D volume data is called short-axis (SAX) view.
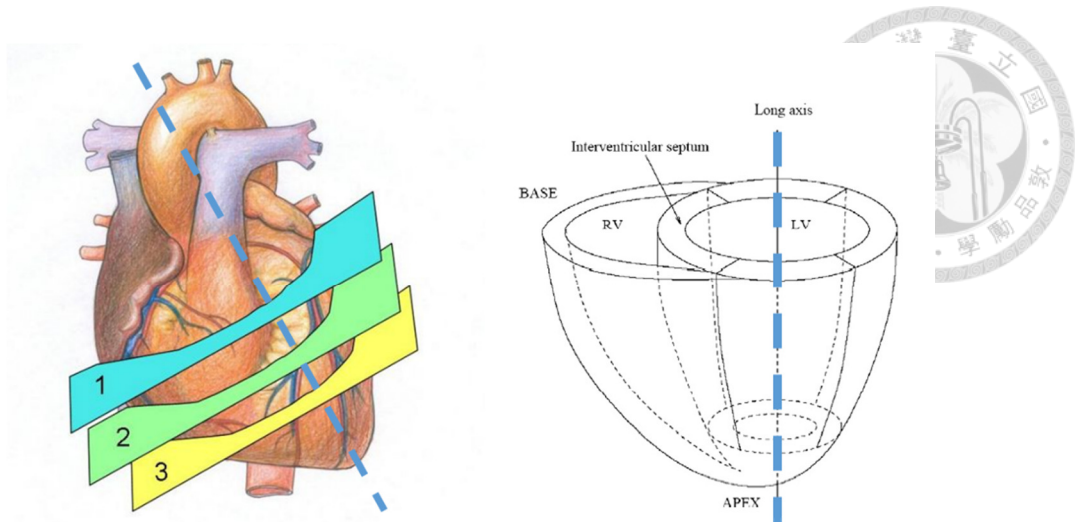
Fig. 2.1   The human heart[1] and its structure[2].

Fig. 2.1 shows the human heart and its long-axis in dashed line. Cutting through Plane 2 reveals the lower two chambers of the heart: the left ventricle (LV) and the right ventricle (RV), shown on the right. The cone-shaped LV is joined by the crescent-shaped RV, with interventricular septum in-between. At the bottom of the ventricles is apex, while at the top of them is the base. Fig. 2.2 shows the MR image of finer structure of the ventricles, acquired in a postmortem examination from the still heart removed from human body. The advantage of SAX view is evident here: the LV exhibits a near circular or oval profile, making it easy to identify. On the inner side of the muscle, the endocardium, of the left ventricle are the papillary muscles and the irregular meaty ridges called trabeculae carneae. These finer structures pose a great challenge in accurate segmentation of the LV, especially when the image is degraded and distorted.

---

[1] Image adapted from

http://web.stanford.edu/group/ccm_echocardio/cgi-bin/mediawiki/index.php/Parasternal_short_axis_view

[2] Image adapted from [7]
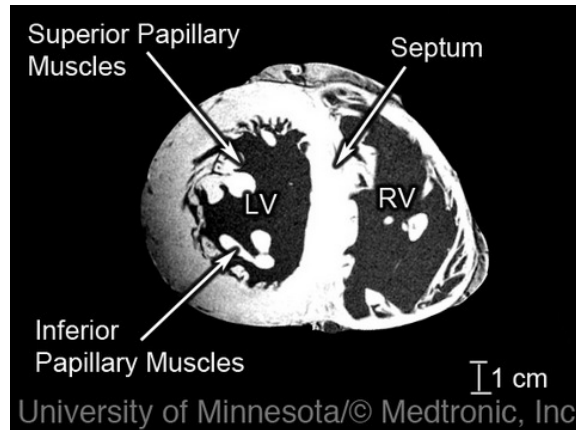
Fig. 2.2 MR image in short-axis view showing finer structure of ventricles[3].

In fact, the actual CMR images acquired from live human body is not up to the same quality (See Fig. 2.3). It has lower signal-to-noise (SNR) ratio and various distortions. A common distortion in MR images is field inhomogeneity. MRI scanner assumes a homogeneous magnetic field within the scan range, therefore, an uneven (i.e., inhomogeneous) magnetic field results in intensity roll-offs in the acquired image. In this case, tissues of the same type may not exhibit the same intensity. This is problematic in general image segmentation tasks because a very basic and logical assumption is that the same tissue type should have similar intensity profile. Another major distortion is the partial volume effect. This happens when tissues to be scanned are finer than MRI scanner's designed resolving power, and it is most prevalent near the boundary of tissues. In the case of CMR images, partial volume effect occurs near the papillary muscles and trabeculae inside the LV cavity.

Fig. 2.4 shows an image stack covering the whole ventricle at a given time. This is the dataset the clinicians will work on to evaluate cardiac functions. As can be seen, the

---

[3] Image courtesy of University of Minnesota.

http://www.vhlab.umn.edu/atlas/cardiac-mri/short-axis-ventricle/index.shtml

LV in those slices vary widely in shape and size. There are a few notable challenges in apical (toward apex) and basal (toward base) slices. In the basal slices, the left ventricle does not form a full circumference and appears to merge into the right ventricle. This protruded area is in fact the left ventricular outflow tract (LVOT), which is connected to great arteries responsible for carrying the blood ejected from the left ventricle. The presence of LVOT in basal slices poses a challenge to existing automated segmentation algorithms; some did not even attempt to process these slices as a result of inherent limitation of their algorithm [10], [19], [25]. On the other hand, in the apical slices, the left ventricle appears to be fuzzy and very ill-defined. The challenge does not stop here: in-between the two extremes, the papillary muscle and trabeculae can occupy almost *all* of the LV cavity and obscure the real endocardium border. This is especially true in the case of hypertrophic cardiomyopathy in end-systolic phase, where the myocardium (heart muscle) and papillary muscle is abnormally thick, leaving very little volume inside the LV cavity.
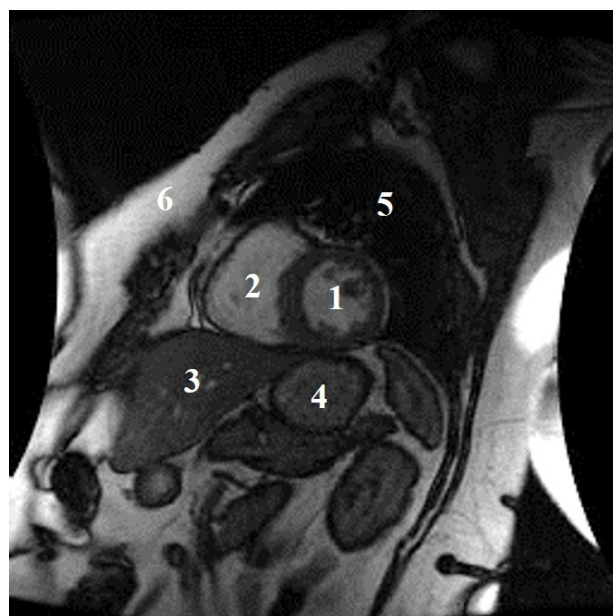
Legend:
1. Left ventricle
2. Right ventricle
3. Liver
4. Stomach
5. Lung
6. Chest wall

Fig. 2.3   CMR short-axis (SAX) view image
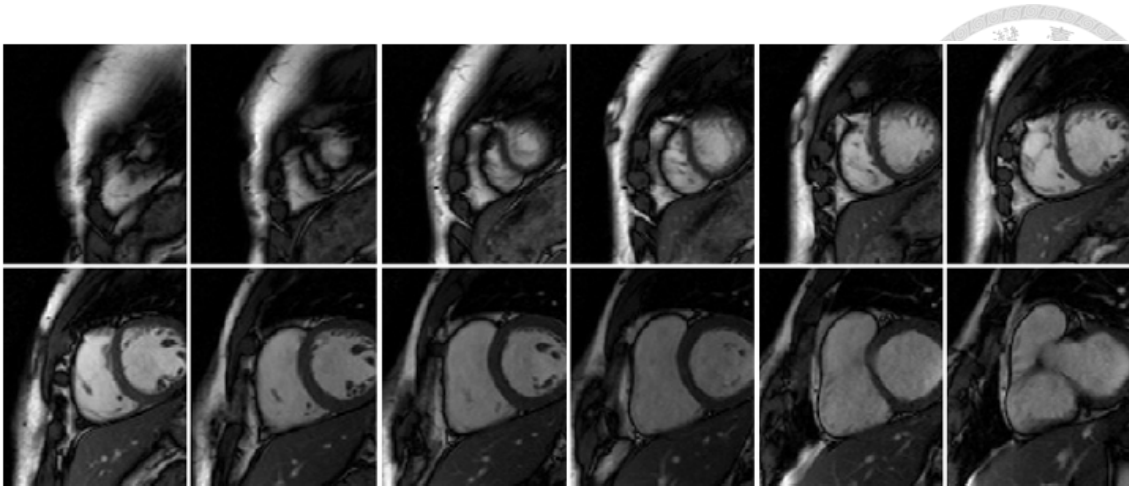
Fig. 2.4   CMR SAX images[4] from the apex (top-left) to the base (bottom right).

2.3   Assessing Left Ventricular Functions

For quantitative assessment of the LV functions, LV endocardial (inner muscle wall) and epicardial (outer muscle wall) contours, either manually-drawn or computer-assisted, are instrumental. Here we introduce some basic parameters that can be derived from these two contours.

Left ventricular volume (LVV) is the blood volume the left ventricle contains. Integrating the voxels enclosed by endocardial contours across the 3D volume gives the LVV. There are two specific moments we are particularly interested in: the moment at maximum blood fill (end-diastole) and the moment at minimum blood fill (end-systole). At end-diastole, integrating the voxels enclosed by endocardial contours across the 3D volume gives **end-diastolic volume (EDV)**. Similarly at end-systole we have the **end-systolic volume (ESV)**.

Stroke volume (SV) measures the blood volume the left ventricle pumps out with each contraction:

---

[4] Image adapted from [7].

$$SV = EDV - ESV \qquad \qquad (2.1)$$

Ejection fraction (EF) measures the proportion of the blood volume the left ventricle ejects into the circulatory system with each cardiac cycle. It is closely related to SV, defined as:

$$EF = \frac{SV}{EDV} \times 100\% . \qquad \qquad (2.2)$$

Left ventricular ejection fraction (LVEF) between 55 up to 70 is considered within normal range in most cases, according to American Heart Association. Any deviation from this normal range may indicate cardiovascular disease [27]. In the case of congestive heart failure, the affected heart does not have the strength to pump blood as efficiently as a healthy heart should. Since less blood is ejected into the circulatory system, a lower than normal EF (under 40) may be observed; it is a strong evidence that the heart's pumping function is impaired due to cardiomyopathy or other causes. A higher than normal EF (above 70) indicates the possibility of hypertrophic cardiomyopathy, in which the myocardium (heart muscle) is abnormally thick and may have problem to completely relax during the diastolic phase, causing smaller EDV and the entailing higher EF.

Left ventricular mass (LVM) is the total muscle mass of the LV. A universally agreed assumption is that interventricular septum (the tissue separating left ventricle and right ventricle) is included as a part of LVM, therefore LVM is calculated by

$$LVM = (EDV_{epi} - EDV_{endo}) \times 1.05 . \qquad \qquad (2.3)$$

Here, EDV_{epi} and EDV_{endo} denote the volume enclosed by epicardial contour and endocardial contour, respectively, at end-diastole. The difference of them yields the volume between the two contours, which is the volume of LV myocardium. LVM is then

12

calculated by multiplying LV myocardial volume with the density of myocardium ($=1.05\text{g/cm}^3$).

Cardiac output (Q) measures the amount of oxygenated blood being circulated throughout the circulatory system. It is the product of stroke volume (L) and heart rate (beats per minute):

$$Q = SV \times HR \tag{2.4}$$

These clinical parameters presented above allow clinicians to access patient's cardiac function. In the next section, we introduce the algorithm that aims to substitute labor-intensive manual segmentation with automated algorithm that aims to aid the clinicians to expedite the evaluation process.

Chapter 3 Proposed Approach

In this chapter, we present the main contribution of this study: the automated left ventricle segmentation.

3.1 System Overview

The block diagram of the system is illustrated in Fig. 3.1. The objective is to delineate the inner muscle wall of the left ventricle, yielding the *endocardial contour*. Inside the muscle wall of the LV is the *LV cavity*. The complete processing flow for delineating the contours will be described in detail, supported by illustrations and diagrams. It can be summarized as three major steps.

First step is LV cavity localization. In this step, we determine the approximate position of the left ventricle. Once the approximate position is known, it then attempts to lock on the center of the left ventricle and creates a circular region of interest (ROI) of variable size, whose diameter depends on the detected left ventricle's diameter. This allows isolating the LV from other unrelated tissues and organs, increasing robustness and segmentation accuracy.

Next, two raw "candidate" endocardial contours are generated. One raw contour is generated based on novel region-based cost-volume filtering (CVF) technique. The other, edge-based Canny's edge detector. These two candidate contours are found to complement one another very well, as both region-based and edge-based segmentation have their own strengths in different parts of the left ventricle.

In the final step, two raw contours are combined in a way that the best sections of

```
                        2D CMR image
                              │
                              ▼
                    ┌──────────────────┐
                    │    LV cavity     │
                    │   localization   │
                    └──────────────────┘
                       │            │
              ┌────────┘            └────────┐
              ▼                              ▼
    ┌──────────────────┐          ┌──────────────────┐
    │      Cost        │          │  Canny's edge    │
    │  initialization  │          │    detector      │
    └──────────────────┘          └──────────────────┘
              │                              │
              ▼                              ▼
    ┌──────────────────┐          ┌──────────────────┐
    │   Cost-volume    │          │      Prune       │
    │  filtering (CVF) │          │      edge        │
    └──────────────────┘          └──────────────────┘
              │                              │
              ▼                              ▼
    ┌─────────────────────────────────────────────┐
    │                 Generate                     │
    │                 contour                      │
    └─────────────────────────────────────────────┘
                          │
                          ▼
    ┌─────────────────────────────────────────────┐
    │                 Correct                      │
    │                 contour                      │
    └─────────────────────────────────────────────┘
                          │
                          ▼
                ┌──────────────────┐
                │     Contour      │
                │     fitting      │
                └──────────────────┘
                          │
                          ▼
                      LV contours
```
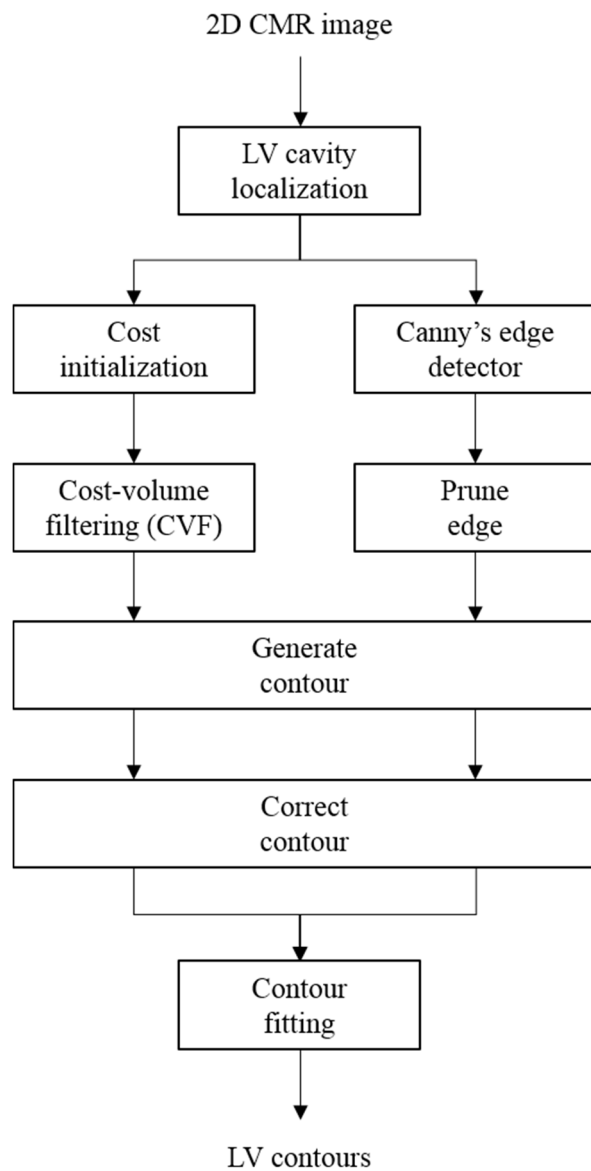
Fig. 3.1   System overview of proposed LV segmentation algorithm

each contour are preserved. The process is automatically determined by the algorithm. In

our implementation, we formulate this as a least square fitting problem, with additional

smoothness term and constraints, yielding the final endocardial contour.

3.2   Left Ventricle Localization

The left ventricular (LV) cavity appears to be a bright circular object in CMR SAX images, whereas the LV myocardium appears darker. Two main stages are involved in locating the left ventricle: 1) The rough position of the LV cavity is determined, and then 2) the region of interest (ROI) is iteratively refined so that the ROI covers the LV, and isolates the LV cavity from all other nearby tissues and organs.

3.2.1   Detection of left ventricular cavity

First stage is rough estimation of LV's position. We can assume that the LV cavity covers the center of CMR image, because the technician would typically operate the scanner such that the LV is at the center of the CMR images. This is true for almost every CMR image we have obtained. If this assumption is violated, our system is designed so that one click onto anywhere inside the LV cavity will suffice. The system will then iteratively refine the ROI covering the LV starting with the initial seed point. This limitation can be easily lifted by incorporating several existing methods [4], [8], [28] that approximates the position of LV in CMR images.

3.2.2   Iterative ROI refinement

The second stage is to iteratively refine the ROI until convergence (See Fig. 3.2 for the evolution of ROI). The steps are described as follows:

1) *Initialization*: Initialize a small search window centered at the location determined in the first stage. In our implementation, we use a 31-by-31 circular shape, which is slightly larger than the size of the LV cavity in apical slices.

2) *Binary thresholding*: Apply binary thresholding in order to identify the LV cavity
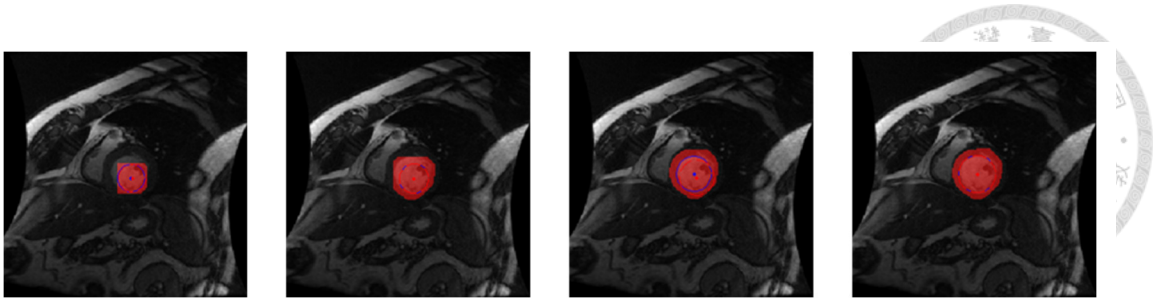
Fig. 3.2　Iteratively compute the ROI until convergence.

within the search window. See the binarized image in Fig. 3.2(b). The threshold

is determined by Otsu's method [15]. It searches for the optimum threshold in the

histogram of the current search window that minimizes the variance within each

class. Otsu's method is designed for images with two distinct classes of signal

intensity, which is ideal to LV cavity detection. For robustness, we accumulate the

histogram over all past iterations. This is because the search window could jitter

wildly and never converge when the optimum threshold varies a lot. Using

histogram accumulation tones down the threshold variation range, and fixes the

problem.

3) *Isolate the LV cavity*: Preserve the connected components that overlap with the

innermost 11-by-11 area. Discard all others. See Fig. 3.4(c). This helps eliminate

the unrelated components in the search window.

4) *Compute the ROI*: Compute the convex hull of the main connected component,

yielding the ROI of current iteration. Calculate its centroid and its size. See Fig.

3.4(e). The purpose is to wrap the papillary muscle and trabeculae (which exhibit

darker intensity profile) in the main connected component so that its centroid is a

meaningful representative of the LV center once convergence is reached.

5) *Check for convergence*: If the centroid *and* the size of the convex hull calculated

in Step 4 does not change, then the LV localization is complete.
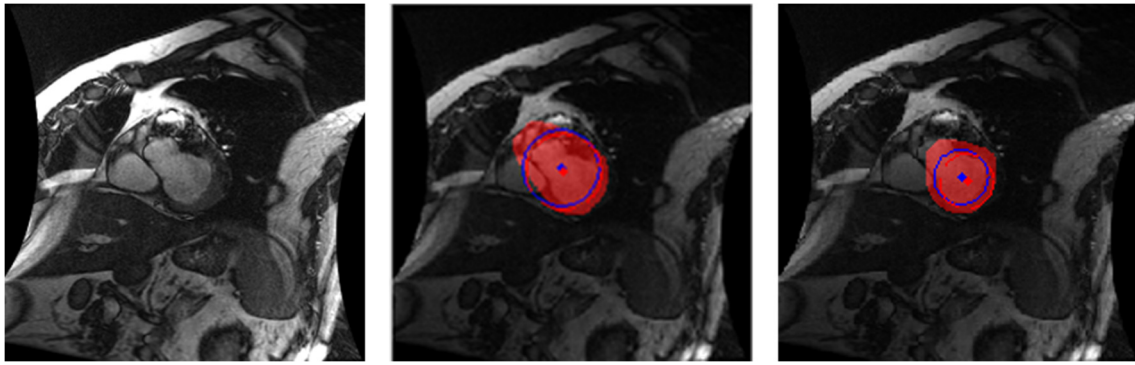
Fig. 3.3   Special attendance in LV localization when LVOT is present *Left*: Presence of LVOT. *Middle*: ROI grows out of range. *Right*: With appropriate stopping criteria. *Red area*: computed search window for next iteration

6) *Next iteration*: The search window for the next iteration is determined by applying morphological dilation on the convex hull using the structure element of size 17-by-17. See Fig. 3.4(d). Proceed to Step 2 for the next iteration until convergence criterion is met.

Additional care for the CMR image with left ventricular outflow tract (LVOT) present is needed. In these images, the connected component (presumably the LV cavity) would extend far beyond the LV region into the RV (See Fig. 3.3). We detect the presence of LVOT based the following two criteria. One is when the center of ROI strays too far away from the original starting position. The other is when the size of ROI exceeds that from last iteration. Though simple, these two criteria combined together can tell whether the ROI grows without signs of stopping. When LVOT detection are triggered, the ROI is reset to its original position and size and proceeds as usual, but with a more strict stopping criteria that halts the iteration prematurely; namely, it now restricts the movement of the ROI within an area of 5-by-5 and any sudden growth will halt the iteration, preventing it from reaching into the non-LV region.
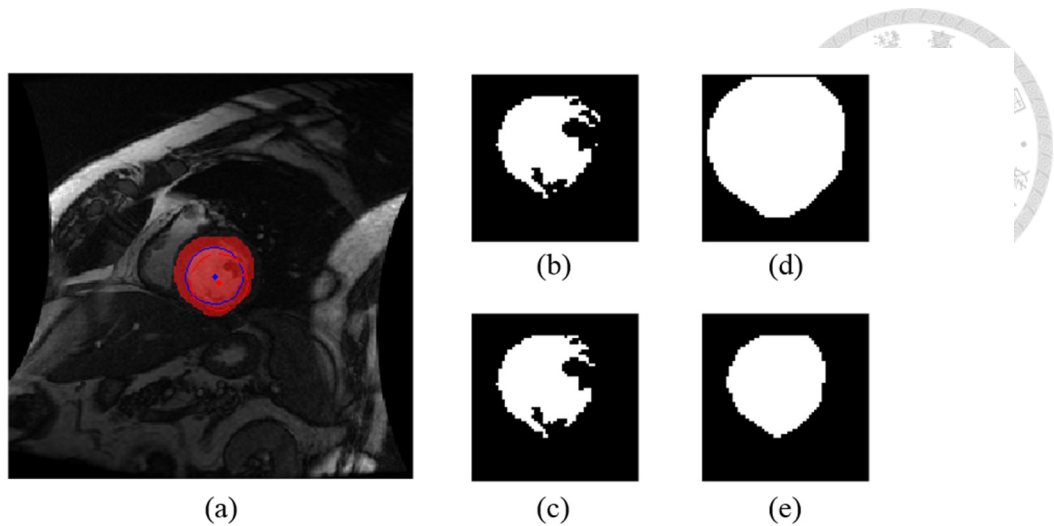
Fig. 3.4　Automatic ROI computation: step-by-step breakdown.

Note that the LV cavity detected at the end this stage, for example the one shown in Fig. 3.4(b), may be a good enough representation of the LV cavity. This is generally not true for all the variants of CMR images, and therefore we introduce a more sophisticated LV endocardium delineation scheme, described in the following section.

3.3　Segmenting LV Blood Pool by Cost-Volume Filtering

Once the region of interest (ROI) covering left ventricle is in place, we can now proceed to segmenting the LV blood pool.

3.3.1　Cost-volume-filtering-based image segmentation

Cost-volume filtering is a filter-based method for multi-labeling problems. It has been shown to be able to achieve computational complexity of $O(N)$ time, which is a very efficient implementation [29]. In general multi-labeling problems, the cost of assigning each label $l \in L$ (e.g., foreground and background) at pixel position (i, j) is first initialized. This yields a 3D cost volume $C(i, j, l)$. Then cross-bilateral filtering is applied
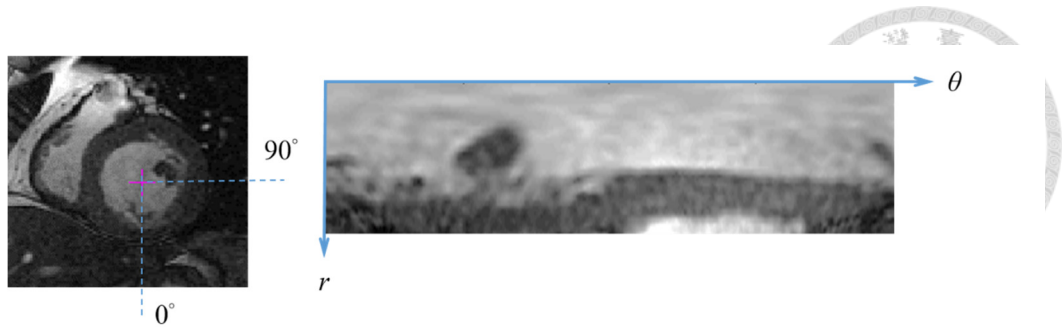
Fig. 3.5 Polar coordinates mapping. *Left*: CMR image. *Right*: After polar coordinate mapping centered at the centroid of LV cavity (marked in a cross)

to the 2D cost slice $C(i, j, l)$ for each $l \in L$. After all the cost slice is filtered, the least costly label is chosen for every pixel, and as a result the filtered cost volume is flattened into 2D CVF-refined label image.

Cost-volume filtering scheme for label refinement is able to achieve spatially coherent[5] results and the label change is aligned with the edges, which makes it ideal for LV cavity segmentation. It was originally used to refine the cost from stereo correspondence matching. Hosni *et al.* first suggested the use of cost-volume filtering in general multi-labeling problem by introducing different cost initialization schemes for each specific application, including the one for interactive image segmentation [29]. However, their cost initialization scheme requires that the operator identify the foreground and background object by free-form drawing, not by automation. Therefore, as will be covered soon, we have designed a completely new scheme for automatically initializing the cost volume. Also, it is specifically tailored to LV blood pool segmentation in order to address the segmentation difficulties caused by partial volume effect.

---

[5] Spatial coherence here refers to connectedness; that labels come in compact, clustered groups.

3.3.2 Polar coordinates mapping

The ROI determined in Section 3.2 is transformed from Cartesian coordinate into polar coordinates, which yields $I_p(i, j)$. See Fig. 3.5. This is very much a standard procedure and has been used in several other works [4], [6], [12], [24], [30]. Since the left ventricular myocardial contour is roughly an oval shape in Cartesian coordinates, mapping it into polar coordinates will produce a flat or a slow-varying curve. This greatly simplify the processing flow and increase robustness because we already know the endocardial and epicardial contours will both be slow-varying curves. Therefore, we can incorporate this prior knowledge as a smoothness constraint in least square fitting of the final result, which is to be discussed in detail in Section 3.4.3.

3.3.3 Cost-volume initialization.

We propose a novel method for automatic cost initialization for CVF-based segmentation in CMR images. First, we calculate a binary image $BI(i, j)$ of the polar image by applying Otsu's method that clusters the pixels into two classes (darker myocardium and brighter LV cavity), where the threshold is calculated from the histogram of the last search window discussed in Section 3.2 (or see Fig. 3.2 for visual example). Only the connected component that overlaps with $r=0$ in the polar image $I_p(r, \theta)$ is preserved because the LV blood pool must cover the centroid of the ROI. Computing the threshold based on the histogram of the last search window instead of a circular ROI is shown to be more robust, as it has one clear advantage: it keeps the unrelated tissues (such as liver, lungs, fats) from contributing to the histogram, or else these unrelated tissues could possibly break the assumption that there are only two distinct classes in the histogram. The bright pixels in

the binary image indicates LV cavity.

The binary image $BI(i, j)$, along with the additional information such as the variance map $VM(i, j)$, are used to automatically initialize the cost volume. See Fig. 3.6 for the information involved in generating the cost volume. A variance map is very suitable for determining the local inhomogeneity, which we will describe its usefulness shortly. The variance map $VM(i, j)$ of the polar image $I_p(i, j)$ is calculated by taking the 7-by-7 window around the pixel at (i, j) and computing its variance by:

$$Var(X) = \frac{1}{N}\sum_{i=1}^{N}(x_i - \mu)^2 . \tag{3.1}$$

We want the cost volume to have certain desirable properties:

1. If the pixel (i, j) in the polar image $I_p(i, j)$ is locally homogeneous (i.e., how uniform the pixel values are), which implies the pixel belongs to either LV cavity or myocardium, then the pixel's label should be harder to change.

2. If the pixel (i, j) in the polar image $I_p(i, j)$ is locally inhomogeneous (i.e., how scattered the pixel values are), which implies that the pixel is near the border of myocardium or near trabeculae, then the pixel's label should be easier to change.

Finally the "foreground slice" in the cost volume is generated using the formula

$$C(i, j, F) = \begin{cases} c - \beta_F \cdot \exp(-\alpha \cdot VM(i, j)) & if\ BI(i, j) = 1 \\ c + \gamma_F \cdot \exp(-\alpha \cdot VM(i, j)) & if\ BI(i, j) = 0 \end{cases}, \tag{3.2}$$

and for the "background slice,"

$$C(i, j, B) = \begin{cases} c + \beta_B \cdot \exp(-\alpha \cdot VM(i, j)) & if\ BI(i, j) = 1 \\ c - \gamma_B \cdot \exp(-\alpha \cdot VM(i, j)) & if\ BI(i, j) = 0 \end{cases}. \tag{3.3}$$

22
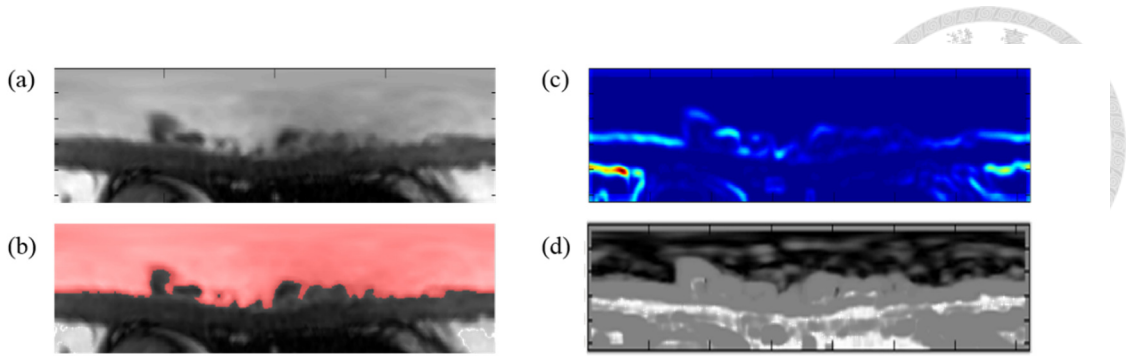
Fig. 3.6 Generating cost volume (a) Polar image of the ROI (b) After Otsu's thresholding and primary connected component extraction, shown in red overlay (c) Variance map of the polar image (d) Generated cost slice for the 'foreground' label.

The c, α, β, and γ are tunable parameters: the parameter c is the constant and it can be set to zero. The parameter α is set as 1000 so that the locally inhomogeneous areas (i.e., the area which exhibits high variance) have more balanced cost between two extremes, making them subject to the cost of its vicinity. The parameters β and γ are the weightings for initializing the cost. We set them as $\beta_F = \beta_B = \gamma_F = \gamma_B = 0.5$ for the most cases. For CMR slices automatically detected as hypertrophic (LV cavity is smaller comparing to normal subjects) the constant c will be adjusted to -20 and the weighting β_B to 20 with the aim of lowering the cost weighting for the LV cavity.

3.3.4 Cost-volume filtering

Once the cost volume is constructed, the next step is to filter the cost volume. More precisely, every slice l of the cost volume $C(i, j, l)$ is filtered by summing a space-variant weighted average of neighboring pixels. Now, given two independent indices $\mathbf{i}=(x, y)$ and $\mathbf{j}=(m, n)$:

$$C'(\mathbf{i}, l) = \sum_{\mathbf{j}} W(\mathbf{i}, \mathbf{j}; I_p)) C(\mathbf{j}, l) \quad \text{for every } l \in L. \tag{3.4}$$

After filtering the cost volume for 100 iterations, we finally choose the label $f_{\mathbf{i}}$ with the least cost for each pixel $\mathbf{i}$ in a winner-take-all fashion:

$$f_{\mathbf{i}} = \arg \min_{l \in L} C'_{\mathbf{i},l}. \tag{3.5}$$

The filter weight $W(\mathbf{i}, \mathbf{j}; I_p)$ is typically given by

$$W(\mathbf{i}, \mathbf{j}; I_p) = \frac{1}{|W|} \sum_{\mathbf{j}} \exp(-\frac{|\mathbf{i} - \mathbf{j}|^2}{\sigma_s^2}) \exp(-\frac{|I_p(\mathbf{i}) - I_p(\mathbf{j})|^2}{\sigma_l^2}), \tag{3.6}$$

where $|W|$ is the normalization factor. Equation (3.4) indicates a cross bilateral filter where the filter weight $W(\mathbf{i}, \mathbf{j}; I_p)$ depends on the spatial closeness between the pixels $\mathbf{i}$ and $\mathbf{j}$ (the first exponential term in (3.6)) and the intensity difference in the guidance image $I_p(\mathbf{i})$ and $I_p(\mathbf{j})$ (second exponential term in (3.6)). Intuitively explained, for each slice, the cost of a pixel at a given position is aggregated from its neighborhoods that have similar signal intensity. The nearer and the closer the signal intensity the given pixel's neighborhoods are, the more the given pixel will be influenced by them.

However, brute force implementation of (3.6) is $O(Nr^2)$ time with filter weight size r. To boost the computational efficiency, we choose to implement CVF with the guided filter proposed by He *et al.*, which is $O(N)$ time and non-approximate [31]. Now, given the guidance image I_p, the filter weight W_{GF} of guided filter is given explicitly by

$$W_{GF}(\mathbf{i}, \mathbf{j}; I_p) = \frac{1}{|\omega|^2} \sum_{k:(\mathbf{i},\mathbf{j}) \in \omega_k} \left(1 + \frac{(I_p(\mathbf{i}) - \mu_k)(I_p(\mathbf{j}) - \mu_k)}{\sigma_k^2 + \varepsilon} \right), \tag{3.7}$$

where k is the index, μ_k the mean, and σ_k^2 the variance of the polar image I_p within the
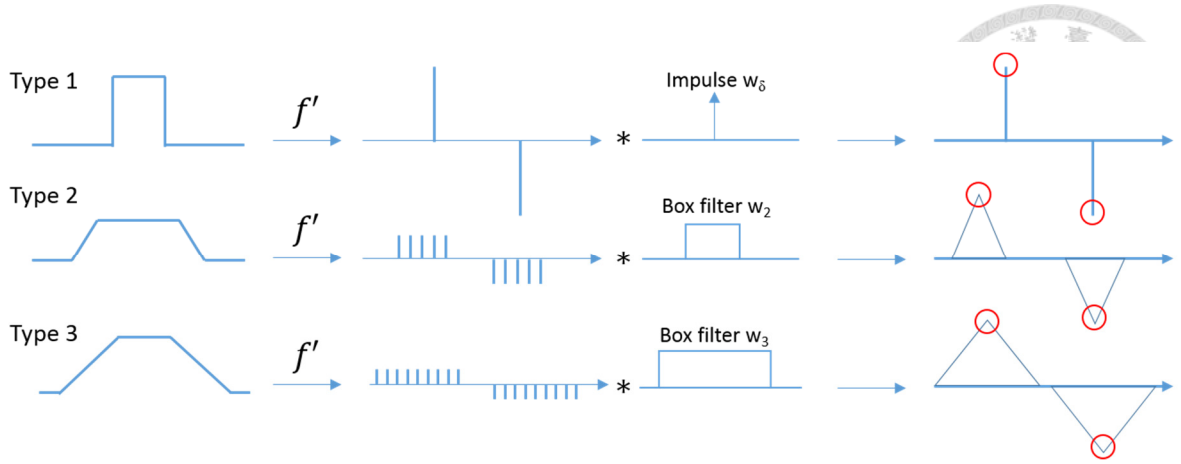
Fig. 3.7   Detection and analysis of contour fluctuations.

window ω that is centered at $\mathbf{i}=(i, j)$, and $|\omega|$ is the number of elements in ω. The parameter ε controls the smoothness of the filtered output. For further explanation of (3.7) refer to [31].
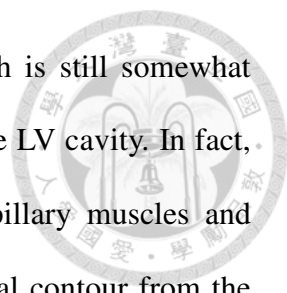
In our implementation, we use (3.7) with window size of 17x17 and $\varepsilon = 10^{-8}$ for filtering the cost slices. Cost-volume filtering is complete after filtering every slice of the cost volume. As mentioned before, we repeat this process 100 times in order to converge the cost. Afterwards, the primary connected component is extracted in the same fashion as in Section 3.3.2.

Up to this point, we have only exploited the region homogeneity of LV blood pool—that we group the pixels presumably belonging to the LV blood pool based on their similarity in signal intensity and their spatial connectedness. Later we will explore the possibility of exploiting gradient information of the image in Section 3.4.2.

3.4   Endocardial Contour Processing

3.4.1   Generating contour from detected LV blood pool

The CVF-filtered binary image is now a 2D representation of the LV cavity where the

cluster of white pixels is where the LV blood pool situates, which is still somewhat premature because LV blood pool is not a good representation of the LV cavity. In fact, LV cavity includes both the LV blood pool and the PMTC (papillary muscles and trabeculae carneae) tissues. In order to generate accurate endocardial contour from the CVF-filtered binary image, we translate this 2D representation of LV cavity into a 1D contour function and correct it.

To generate the contour function, denoted as f, we project vertical rays upwards from below the binary image. When the individual ray hits the major connected component, the ray stops. The hit spots are translated into a one-dimensional contour function f, in which the x-axis denotes the angle and the y-axis denotes the distance to the centroid (determined in ROI localization step).

The contour function f will have some abrupt fluctuations, which occurs mostly where the PMTC are present. The fluctuation's exact onset and termination can clearly be determined once we derive the first-order derivative f' of the contour function. See Fig. 3.8 for visual illustration. It is obvious that the spikes in f' occurs with the presence of PMTC. Since the PMTC is, by convention, a part of the LV cavity, we will regularize the contour function in order to align the contour function closely with the endocardium. Therefore, the preliminary contour correction is introduced. It involves two steps: First, the onset and the termination of each fluctuation are detected. Second, the fluctuation is substituted with linear interpolation.

The main idea of detecting the fluctuations is illustrated in Fig. 3.7. Depending on test subject's heart health and anatomic variations, there are several types of fluctuations which can be observed in the contour function. *Type 1 fluctuations* exhibit sharp changes in both onset and termination. To detect Type 1 fluctuations, we calculate the first-order derivative f' of the contour function. The resultant output will have positive and negative
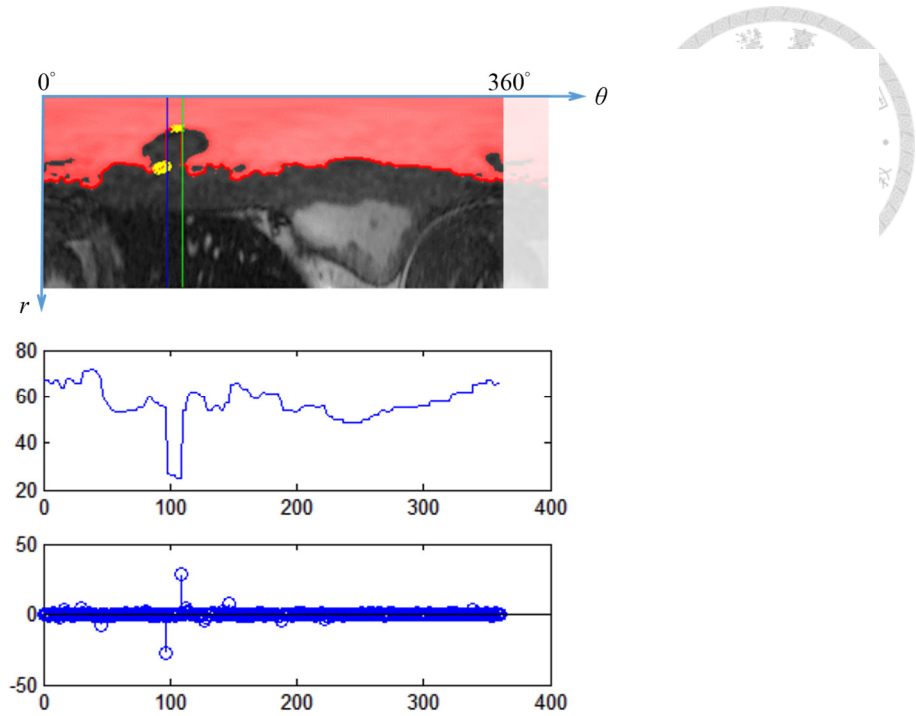
Fig. 3.8   Contour function fluctuations in relation with its first-order derivative (Top)

Polar image of the ROI with LV cavity marked in overlay. (Middle) Contour function

of the LV cavity. (Bottom) First-order derivative of the contour function

spikes representing onset and termination, respectively (illustrated in Fig. 3.7). However,

the spikes are recognized as onset and termination only if each one's absolute value

exceeds a certain threshold t_1. *Type 2 fluctuations* exhibit less abrupt changes than Type

1 does, and their first-order derivative are less significant. To detect Type 2 fluctuation,

the first-order derivative is convoluted with a box filter of unit height and width w_2. The

resultant output will have hill- or triangle-like responses. The local maximum and

minimum are picked up as onset and termination only if each one's absolute value exceeds

a certain threshold t_2. *Type 3 fluctuations* occur mostly in subjects with thicker PMTC

tissues. Since they are much smoother in appearance than the previous two types, we use

a wider box filter with unit height and width w_3. The onset and termination is determined

in the same fashion with a threshold value of t_3. All the threshold values and box filter
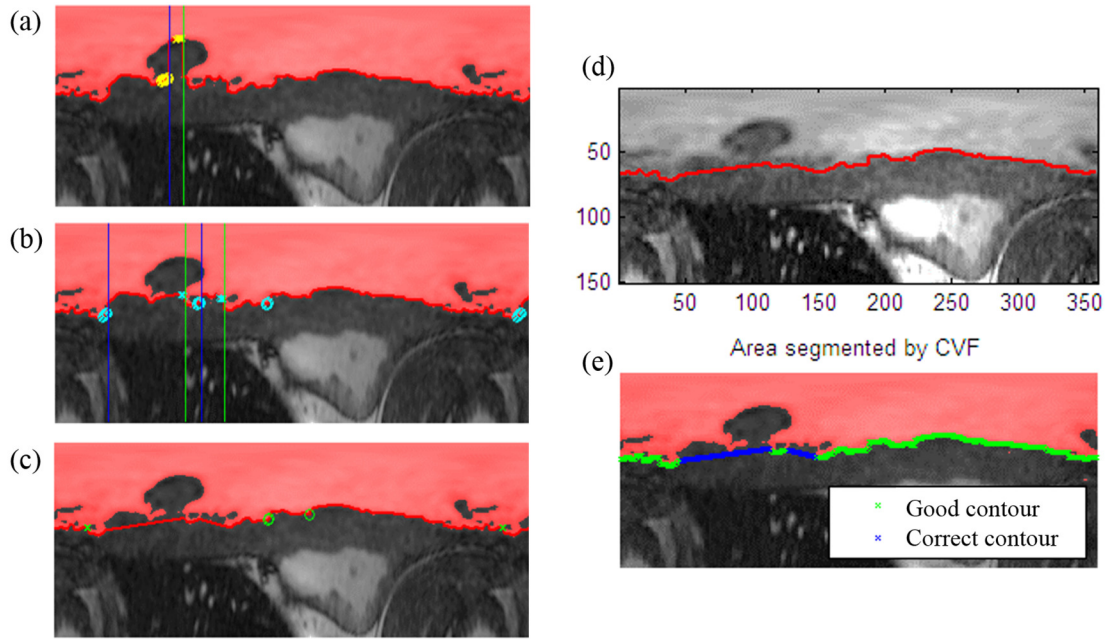
Fig. 3.9 Demonstrating contour function correction (a)(b)(c) Correcting the curve in successive order. Label 'O' on the curve denotes candidate onset and 'X' denotes candidate termination. Bounded by vertical lines are detected fluctuations. (d) Corrected contour (e) Corrected contour superimposed with CVF-based segmentation result.

widths are determined experimentally.

The fluctuations exhibit a pattern in which the onset and termination come in pairs and in order. That is, an onset, by definition, always entails a termination; the reverse is not true. If the position of onset and that of termination are denoted as x_0 and x_1, respectively, then the contour f in the interval $[x_0, x_1]$ is corrected by connecting a straight line through $f(x_0)$ and $f(x_1)$, namely:

$$g(x) = f(x_0) + [f(x_1) - f(x_0)]\frac{x - x_0}{x_1 - x_0} \quad for \ x \in [x_0, x_1], \tag{3.8}$$

where g is the corrected contour function. The contour function goes through Type 1, 2, and 3 detectors in successive order, and (3.8) is repeated for each interval found. At the

28

same time, we maintain a set that records the contour segments that have been corrected, which is denoted as *SetCorrected*.

The pseudo code for correcting the contour function is summarized in Table 3.1 and the complete workflow and the resulting output is illustrated in Fig. 3.9.

Generate the contour function f
Initialize *SetCorrected* as a null set
$f' \leftarrow$ derivative of f
for each detector i:
    Convolute f' with box filter w_i
    if both the absolute value of local extrema $> t_i$
        $x_0/x_1 \leftarrow$ position of positive/negative extrema
        Linear interpolation by (3.8)
        $SetCorrected \leftarrow SetCorrected \bigcup [x_0, x_1]$
    end if
end for

Table 3.1 Pseudo code for contour function correction

3.4.2 Complementary contour generation

The contour segments that were corrected using simple linear interpolation in the last step may not match closely enough with the desired endocardial contour. To overcome this, we utilize the gradient information of the image because high gradient magnitude response can be observed along the endocardium. Exploiting this fact allows us to complement the contour segments B with these additional information, further improving the accuracy of the detected contour.

In our attempt to exploit gradient information, we choose Canny's edge detector [32] because it suppresses non-maximum gradient response and works well over a wide range of MR images. However, not only the endocardial contour responds to Canny's edge
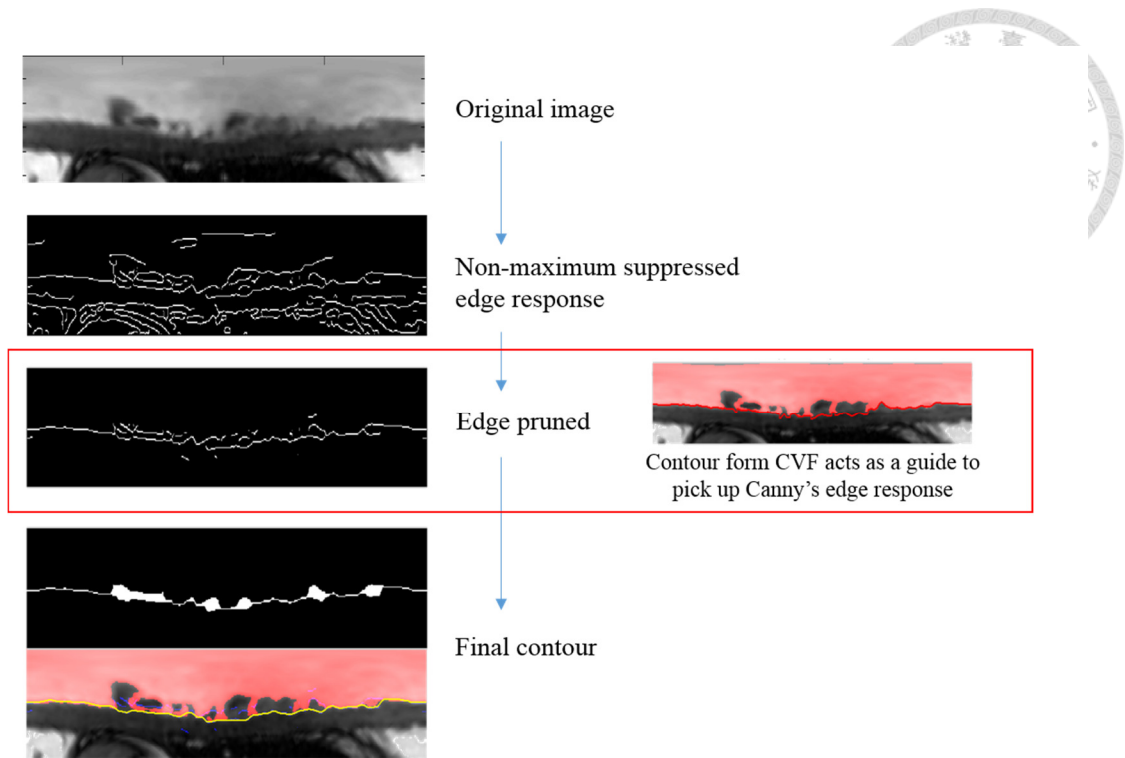
Fig. 3.10 Workflow of complimentary contour generation

detector, other tissues, PMTC in particular, and MR distortions could also return false positives that lead to erroneous results. To extract the endocardial contour from the rest of the edge responses, we use the contour generated based on CVF after contour correction to act a guide. See Fig. 3.10 for the workflow. The guide picks up nearby edge responses generated by Canny's edge detector. Finally, the picked-up edge response is refined through a process of discarding connected components that are less than 16 elements, and employing morphological closing operation with circular structure element of radius 10. The refined edge response is then transformed into a contour function (refer to Section 3.4.1 for contour function generation) and is denoted as f_c, the complementary contour function. Similar to the contour function generated by CVF-based segmentation result, the complementary contour function f_c also has some fluctuations due to lack of sufficient edge information, and is corrected in the same manner as described in Table 3.1.
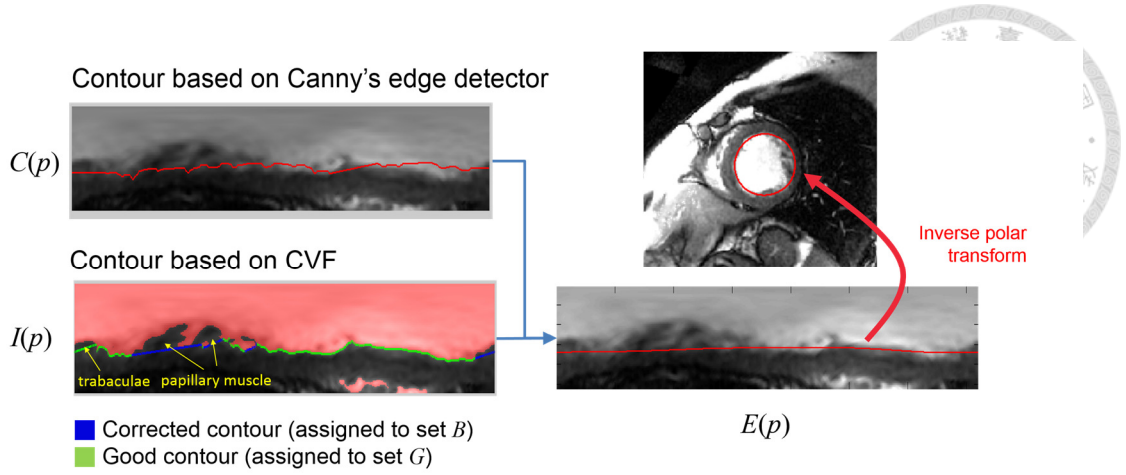
Fig. 3.11 Workflow of endocardial contour regularization

3.4.3 Endocardial contour regularization

In this step, we propose a regularization step in order to incorporate the information gathered from region-based (Section 3.3.4) and gradient-based (Section 3.4.2) methods from CVF and Canny's edge detector, respectively. Specifically, two raw contours obtained from region-based CVF and gradient-based Canny's edge detector undergo a combination and smoothing process during which suitable weighting function for each raw contour are determined and additional constraints are enforced.

Let us denote I as the contour generated from CVF-based segmentation after contour correction, C as the complementary contour generated from Canny's edge detector after contour correction. Now, we want to obtain a final regularized endocardial contour E, where the regularization is done by minimizing the following objective function:

$$\min O(E) = \sum_{p \in B} \left[E(p) - C(p)\right]^2 + \sum_{p \in G} \left[E(p) - I(p)\right]^2 + \lambda \sum_{p} \left[E''(p)\right]^2 \tag{3.9}$$

subject to

$$E(p) > I(x) \quad \forall p , \tag{3.10}$$
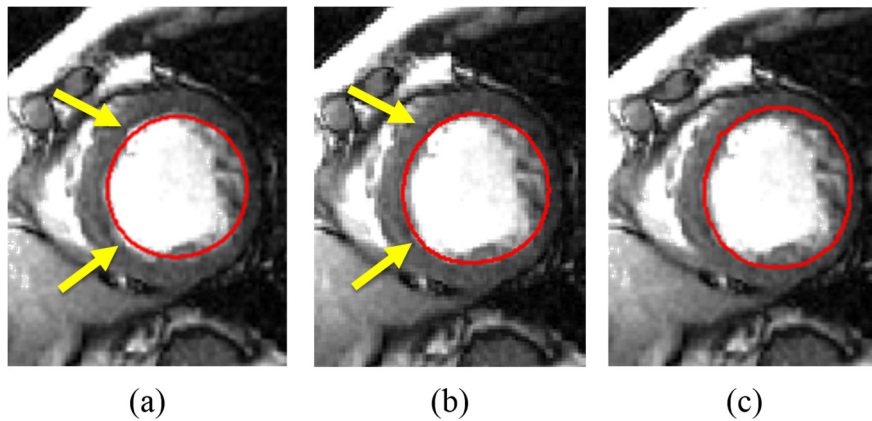
Fig. 3.12 Comparison of segmentation results (a) Auto without constraint (b) Auto

with constraint. Notice the improved accuracy. (c) Expert-drawn.

where the set B is the set of the CVF-based contour segments that have been corrected,

set G is the set of the CVF-based contour segments that do not require correction, and is

equivalent to the complement of the set B. The workflow is illustrated in Fig. 3.11. The

rationale of using the complementary contour only at the set B is because Canny's edge

response is generally less reliable because it sometimes returns false positive edge

responses. However, when discerning the fine edge response between the endocardium

and PMTC tissues, Canny's edge detector is more suitable in doing so.

As shown in (3.9), the final endocardial contour E is driven by two factors: the data

term (first two terms) and the smoothness term (the third term). Since the objective

function is a cascade of quadratic terms summed together, minimizing it becomes an

effort to make every term as close to zero as possible while fulfilling some constraints

specified in (3.10). The data term tries to minimize the error between the final contour

and the two contour functions at specific segments dictated by set B and G. The

smoothness of the final endocardial contour is done by minimizing second-order

derivative of the final contour itself, where the degree of smoothness is controlled by

weighting λ. Furthermore, the additional constraint in (3.10) ensures that the final endocardial contour E fully encloses the LV cavity (see Fig. 3.12), represented by the contour I generated from CVF-based segmentation result. This additional constraint is designed to fully enclose PMTC tissues as well as the LV blood pool inside the final endocardial contour. In our experiments, we set λ=1000 because it has a good balance between over-smoothing and minimal smoothness.

3.5   Cardiac Cycle Determination

To derive left ventricular ejection fraction (EF), one needs to determine the end-systolic volume (ESV) and end-diastolic volume (EDV), which in turn requires the time moment when end-systolic (ES) phase and end-diastolic (ED) phase occur. This can be determined automatically by the proposed method. After integrating the voxels within the endocardial contour, we are able to compute the left ventricular blood volume over time. The ES phase is then designated by the time moment of minimum blood volume, and the ED phase the time moment of maximum blood volume. While ES and ED can be determined automatically by the proposed method, other methods such as ECG signal is also possible.

Chapter 4 Results and Discussion

4.1 Test Dataset and Evaluation Metrics

We adopt an open test dataset provided by Sunnybrook Health Science Center at Toronto, Canada [33] for evaluating the performance of the proposed algorithm. The dataset provides CMR scans acquired from 45 patients encompassing one healthy and three distinct pathological cases (see Table 4.1). Endocardial contours at both end-systole and end-diastole drawn by experienced cardiologists are provided, as well as the source code for evaluating the performance of the segmentation results. Technical details regarding the test CMR datasets are:

- Acquisition protocol: Steady-state free precession (SSFP) MR short-axis view (SAX) images are obtained during 10-15 second breath-holds with a temporal resolution of 20 cardiac phases over the heart cycle, and scanned from the end-diastole. Six to 12 SAX images were obtained from the atrioventricular ring to the apex.

- MRI scanner: 1.5T GE Signa MRI with field of view=320mm*320mm, matrix=256*256, slice thickness=8mm, gap between slices=8mm.

Case	Subject's pathology	# of subject
SC-N	Healthy	9
SC-HF-I	Heart failure with infarction	12
SC-HF-NI	Heart failure with non-ischemic disease	12
SC-HYP	Hypertrophy	12

Table 4.1 Pathological cases in the adopted test dataset
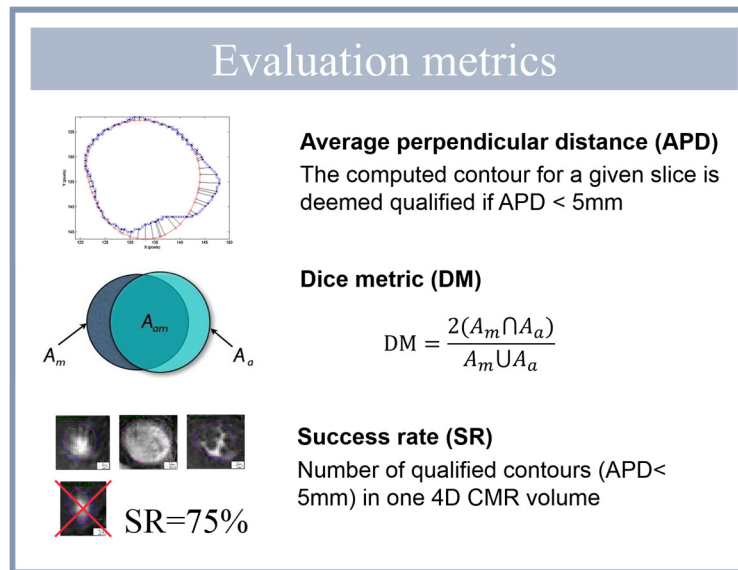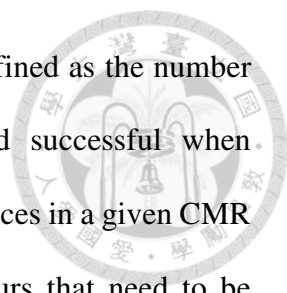
Fig. 4.1　Summary of evaluation metrics used in CMR segmentation results

Given an automatically computed contour A and manually drawn contour M, two metrics depicting how close these two contours relate to one another are:

- Average perpendicular distance (APD), which measures the absolute distance from any given point in contour A to contour M in the direction of its normal vector, averaged over all points in contour A. It can be interpreted as mean absolute error from the gold standard. Therefore, lower APD indicates better segmentation accuracy.

- Dice metric (DM), which measures the proportion of the overlapped area of A and M over the union of A and M. The value of DM is always between 0 and 1. A higher DM typically implies a closer match between the two contours, but it is not necessarily true, as will be discussed later in this chapter. Define A_X as the area enclosed by contour X, DM of two contours is defined as:

$$DM = \frac{2(A_A \cap A_M)}{A_A \cup A_M}.$$
(4.1)

Also important is the third evaluation metric: success rate (SR)[6], defined as the number of successfully detected contours (computed contour is deemed successful when APD<5mm) over the total number of contours from apical to basal slices in a given CMR scan. Therefore, the higher the success rate, the less failed contours that need to be manually corrected. These three evaluation metrics are summarized in Fig. 4.1. Success rate has been somehow overlooked in previous literature [7], where some seemingly high accuracy segmentation results that are reported by previous works are blinded by the fact of omitting certain amount of CMR slices (e.g., more problematic basal and apical slices), making the result appears better. It is important that all three metrics must be considered as a whole when evaluating the performance of CMR segmentation algorithm.

4.2 Evaluating Segmentation Results
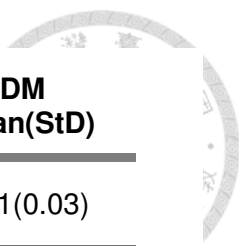
All 45 patients' CMR volume at ED and ES phases, which is a total of 800 images, are used to evaluate the proposed method. Of which 52 (approx. 6.7%) computed endocardial contours are rejected by the evaluation tool due to high APD (>5mm).

Performance analysis shows that the proposed method for delineating LV endocardial contour achieves high success rate (SR) of 94.1±6.1%. Average perpendicular distance (APD) and dice metric (DM) read 1.75±0.42mm and 0.91±0.03 respectively, which implies the automated LV segmentation results are not only robust, they also match closely to the gold standard. Table 4.2 confirms that the proposed method is one of the most competitive among recent works[7]. In particular, the proposed method

---

[6] In some literature, the success rate (SR) is alternatively named "good percentage."

[7] As regulated by the evaluation tool, rejected contours are not included in the statistics of APD and DM.

Method	SR (%) Mean(StD)	APD (mm) Mean(StD)	DM Mean(StD)
Huang 2011 (auto) [10]	81.5(18.0)	2.19(0.44)	0.91(0.03)
Hu 2013 (auto) [14]	91.1(9.4)	2.24(0.40)	0.89(0.03)
Constantinides 2012 (semi-auto) [16]	91.0(8.0)	1.94(0.42)	0.89(0.04)
Constantinides 2012 (auto) [16]	80.0(16.0)	2.44(0.56)	0.86(0.05)
Ngo 2013 (semi-auto) [34]	**97.9(6.18)**	2.08(0.40)	0.90(0.03)
Ours (auto)	94.1(6.1)	**1.75(0.42)**	**0.91(0.03)**

Table 4.2   Performance comparison of proposed method. All results listed are evaluated by the same Sunnybrook CMR database consisting of 45 patients.

	SR (%)		APD (mm)		DM	
Group	Mean	StD	Mean	StD	Mean	StD
SC-HF-I	94.2	7.7	1.542	0.296	0.93	0.02
SC-HF-NI	95.1	4.1	1.736	0.459	0.92	0.02
SC-HYP	93.6	6.5	1.900	0.420	0.88	0.03
SC-N	93.4	5.3	1.834	0.377	0.89	0.02
Overall	94.1	6.1	1.748	0.417	0.91	0.03

Table 4.3   Evaluation of proposed method on each of the four groups plus all 45 patients.

has the best APD and DM among all recent methods. The SR ranks slightly behind the method proposed by Ngo *et al*. It is noteworthy that only the methods from Huang 2011, Lu 2013, and Constantinides 2012 (auto) are automatic. Others require either drawing a rough initial contour or annotated datasets for training the prior models. By contrast, the
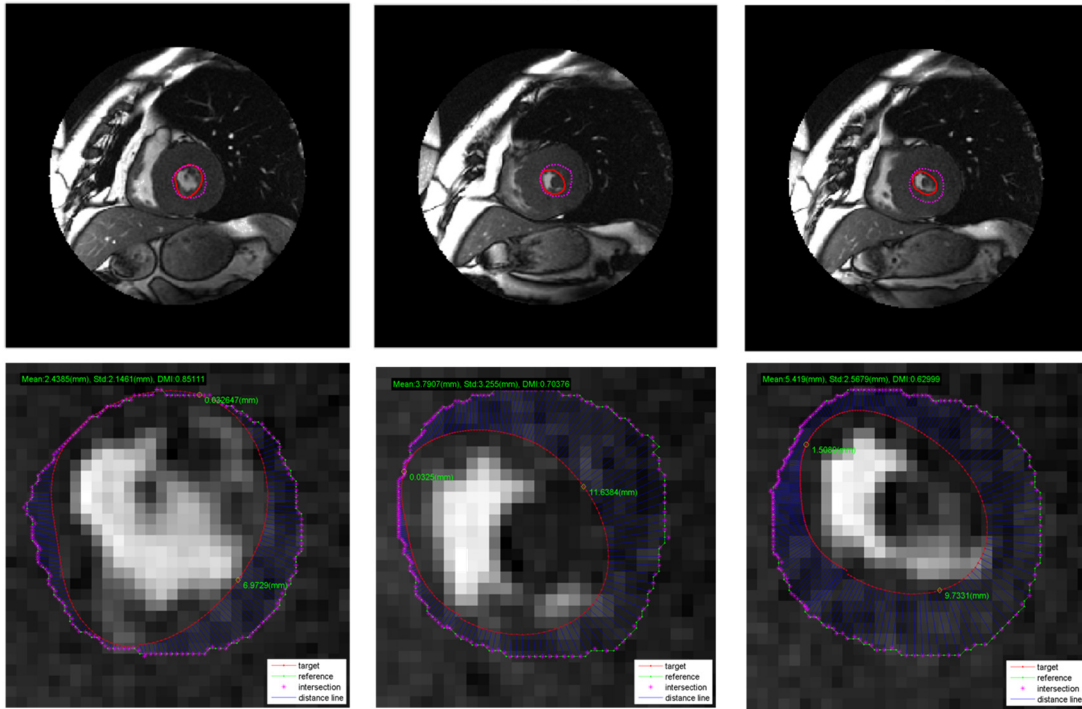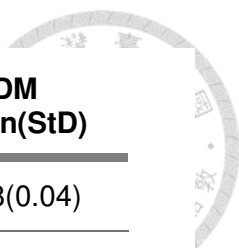
Fig. 4.2 Selected slices at ES phase showing segmentation result for the case of hypertrophy (SC-HYP-08). Top row shows computed contour (red solid line) versus manually-drawn contour (purple dashed line). Bottom row shows close range view of the region of interest.

proposed method requires no training; we only ask the operator for one click on anywhere inside the LV cavity if the assumption that the LV lies near the center of MR images is violated. For streamlining the evaluation process, however, this initial knowledge is provided by the operator for every MR image. This prerequisite can be easily removed if we adopt existing algorithms [4], [8], [28] that locate the rough position of the LV to replace the simple manual initialization step. Therefore, we believe it is sufficient to claim the proposed method is fully automatic. By this regard, the proposed method is currently the top performer comparing to all other automatic methods.

Table 4.3 looks into the performance variation for each pathological group. The performance of the proposed method is not sensitive to any particular pathological group,

Method	SR (%) Mean(StD)	APD (mm) Mean(StD)	DM Mean(StD)
Jolly 2009*	95.62(8.83)	2.26(0.59)	0.88(0.04)
Lu 2009*	72.45(18.86)	2.07(0.61)	0.89(0.03)
Huang 2009*	--	2.10(044)	0.89(0.04)
Wijnhout 2009*	86.47(11)	2.29(0.57)	0.89(0.03)
Constantinides 2009*	92.28(--)	2.04(0.47)	0.89(0.04)
Marák 2009*	--	3.00(0.59)	0.86(0.04)
Feng 2013	92.8(9.2)	1.93(0.37)	0.86(0.04)
Ngo 2013	**96.58(3.66)**	2.22(0.46)	0.89(0.03)
Ours	96.31(4.85)	**1.67(0.40)**	**0.91(0.03)**

Table 4.4 Performance comparison with Sunnybrook CMR "validation" set consisting of 15 patients (N=3, HYP=4, HF-I=4, HF-NI=4). Results published in the MICCAI 2009 Challenge are marked by asterisk (*).

though it can still be observed that the APD for the group of heart failure (SC-HF-I and SC-HF-NI) is the lowest while APD for the group of hypertrophy (SC-HYP) is slightly higher. The reason explaining this finding is because hearts afflicted by heart failure often have clearly defined endocardial contour across all time phases, therefore it is easier to be detected accurately. In extremely hypertrophic cases, by contrast, the LV blood pool at ES phase can barely be seen—a result of an abnormally thick muscle wall that leaves little chamber volume for blood fill. See Fig. 4.2 for example of a hypertrophic case we encountered. The leftmost image shows sub-par yet still acceptable segmentation result, in which a portion of the endocardial contour can still be seen. As the MR scanning plane goes further down the slices (from left to right), papillary muscles and trabeculae carneae (PMTC) begin to obscure *all* of the endocardial contour, and the proposed method also

begins to fail. In the rightmost image in Fig. 4.2, the segmentation result is rejected mainly due to the fact that the PMTC tissues are so densely collapsed together that no endocardial contour can be seen. Of course, by tracing the motion of the muscle wall over time, it is possible to recover the endocardial contour even if it is completely obscured. It is however beyond the design of the proposed method. Nevertheless, tracing the motion of the muscle wall is a very interesting and highly practical way of improving the segmentation accuracy. We leave it for future works.

Table 4.4 lists the result comparison[8] using a portion of the Sunnybrook CMR database. This portion is the "validation" set, on which all the published results of the competing methods in MICCAI 2009 Challenge are based. Again, the proposed method outperforms all other competing methods in terms of APD (1.67±0.40mm) and DM (0.91±0.03). In summary, strong evidences lead us to believe that the proposed method is one of the most competitive method among current state-of-the-arts.

4.3   Evaluating Left Ventricular Functions

Cardiac parameters extracted from the CMR volume are the most relevant information to clinicians. The proposed method answers this need: it also provides accurate assessment of the left ventricular parameters derived from the intermediate automatic segmentation. The mean bias between automatically versus manually computed ejection fraction (EF) over all 45 patients is 1.61±4.72. Mean bias between automatically versus manually computed end-systolic volume (ESV) and end-diastolic volume (EDV) are minus

---

[8] Likewise, all methods [11], [12], [17], [34]–[37] listed in Table 4.4 follow the principle that the rejected contours are not included in the statistics of APD and DM.

	EF error		ESV error (mL)		EDV error (mL)	
Group	Mean	StD	Mean	StD	Mean	StD
SC-HF-I	-0.15	2.89	-8.56	13.23	-10.65	18.64
SC-HF-NI	2.27	4.64	-11.11	10.76	-8.45	17.66
SC-HYP	2.13	5.01	-6.49	7.93	-10.94	12.89
SC-N	2.39	5.70	-1.07	4.69	1.71	14.68
Overall	1.61	4.72	-7.19	10.53	-7.67	16.92

Table 4.5 Evaluating cardiac parameters with respect to each pathological group.

7.19mL±10.53mL and minus 7.76mL±16.92mL, respectively.

.   Refer to Table 4.5 for detailed error analysis for each pathological group. The mean bias of EF is almost negligible for all four pathological groups as well as for the overall evaluation. On the other hand, the computed ESV and EDV have an almost universal, but slight, negative bias regardless of pathological groups. This is an expected consequence: due to segmentation error, the computed endocardial contour often lies inside the manually annotated endocardial contour (a clear example is shown in Fig. 4.2). As a result, the proposed algorithm tends to underestimate the ESV and EDV. However, the tendency to underestimate the LV blood volume is consistent enough, therefore the bias will be negated when computing the EF (because estimating EF involves the difference of EDV and ESV; refer to Section 2.3). This is confirmed by Bland-Altman analysis[9] shown in

---

[9] Bland-Altman analysis compares the value X from a new measurement techniques against a reference value Y. The *x*-axis is the mean (X+Y)/2 and the *y*-axis is the residual X-Y. In this case, the value X is the computed cardiac parameters and Y is the gold standard. The smaller the residual, the higher the agreement between two measurement techniques.
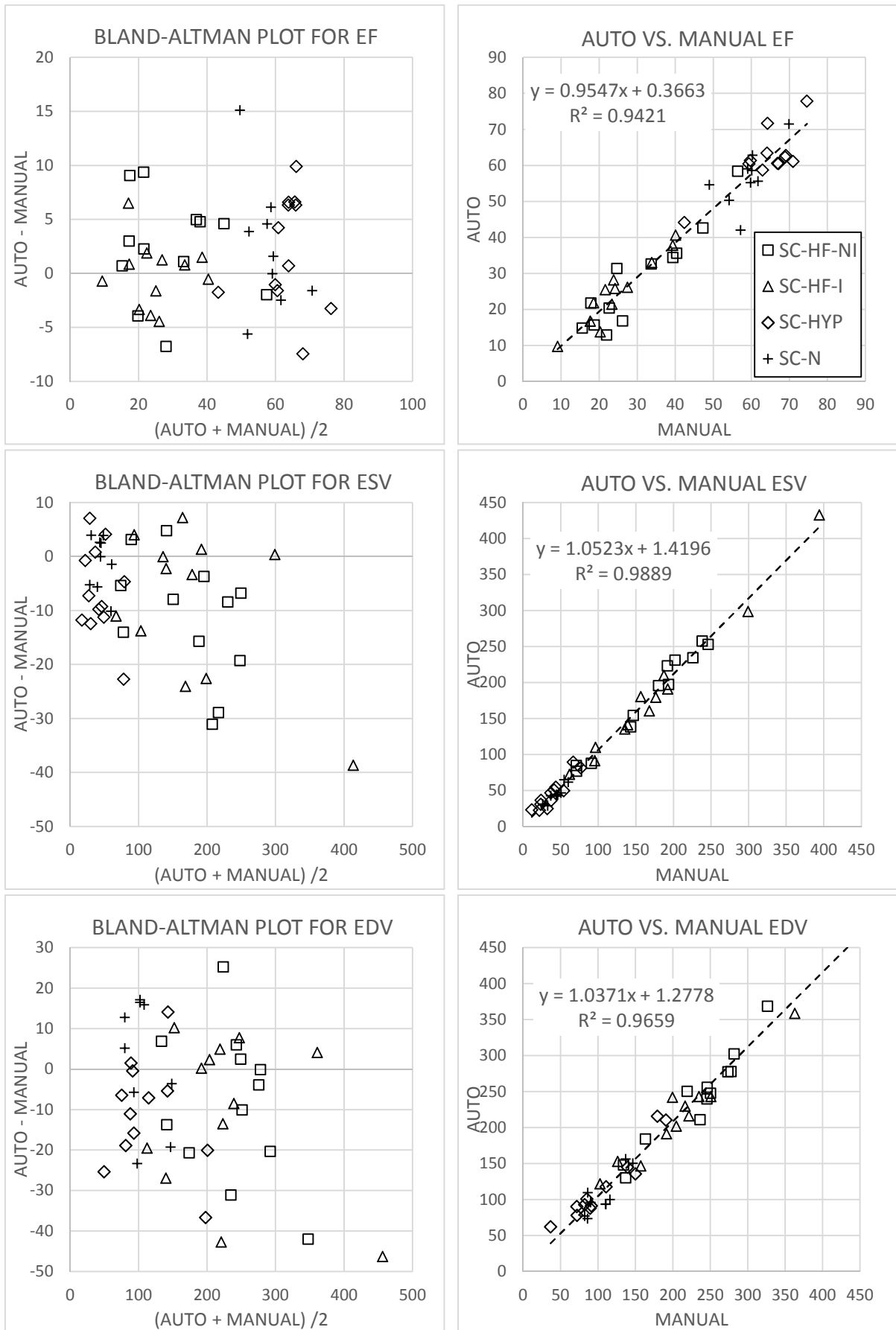
Fig. 4.3   Bland-Altman analysis (left) and regression analysis (right) of cardiac parameters.
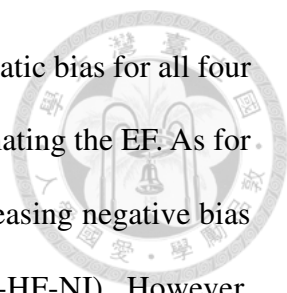
Fig. 4.3, left column. Bland-Altman analysis for EF shows no systematic bias for all four pathological cases, which makes the proposed method ideal for estimating the EF. As for the computed ESV and EDV, the Bland-Altman analysis shows increasing negative bias as mean value increases for heart failure cases (SC-HF-I & SC-HF-NI). However, evaluation of the segmentation results already confirms the proposed method achieves the best APD and DM in heart failure cases. What causes the seemingly contradicting evidences? The reason behind this discrepancy can be explained: depending on the LV cavity size, a small segmentation error may result in large difference in terms of the segmented area, and ultimately, the LV blood volume. This effect can be further amplified when dealing with enlarged LV cavity, which is exactly the case for patients suffering from heart failure, whose heart chambers are usually pathologically oversized. In the Bland-Altman plot, one can observe that data points deviating from the ideal reference line (y=0) are exclusively heart failure cases (note that not all heart failure cases show the same amount of bias). Given the above findings, we conclude that the bias for ESV and EDV is approximately proportional to the mean of two measurements. For EF, a negligible bias is observed, and the measurement error is consistent across all range.

Regression analysis shows strong correlation between automatically and manually computed cardiac parameters, shown in Fig. 4.3, right column. Coefficient of determination (R^2) between automatically and manually obtained EF, ESV, and EDV are 0.94, 0.99, and 0.97, respectively. Other reported R^2 for EF, while not necessarily using the same database for evaluation, are: 0.87 by Cocosco *et al.* [8], 0.90 by Lu *et al.* [6], 0.92 by Lorenzo-Valdés *et al.* [25], 0.92 by Cordero-Grande *et al.* [38], and 0.83 by Constantinides *et al.* [16]. This is a strong evidence that the proposed method achieves top-of-the-line result. The above results are organized in Table 4.6.

Method	R^2 for EF
Lorenzo-Valdés 2004	0.92
Cocosco 2008	0.90
Cordero-Grande 2011	0.92
Constantinides 2012	0.83
Lu 2013	0.92
Hu 2013	0.938
Ours	**0.942**

Table 4.6 Reported coefficient of determination R^2 for EF.

Aside from these EF, ESV, and EDV, it is also possible to evaluate peak ejection rate (PER) and peak filling rate (PFR). However, the database that we adopted provides only the gold standard contours at ES and ED phases, therefore we do not have a true reference value. Nevertheless, we are optimistic that it will yield accurate results too given the high performance of the proposed method, shows the evaluation and the results presented above.

4.4 Discussion

The main advantage of the proposed method is the ability to negate the effect of PMTC tissues effectively through the proposed myocardial contour processing steps. The effectiveness is backed by the CVF-based image segmentation, which is able to detect most of the LV blood volume while being resistant to artifacts affecting the MR images such as field inhomogeneity and partial volume effect. First, we would like to discuss these two artifacts and how CVF is able to overcome them.
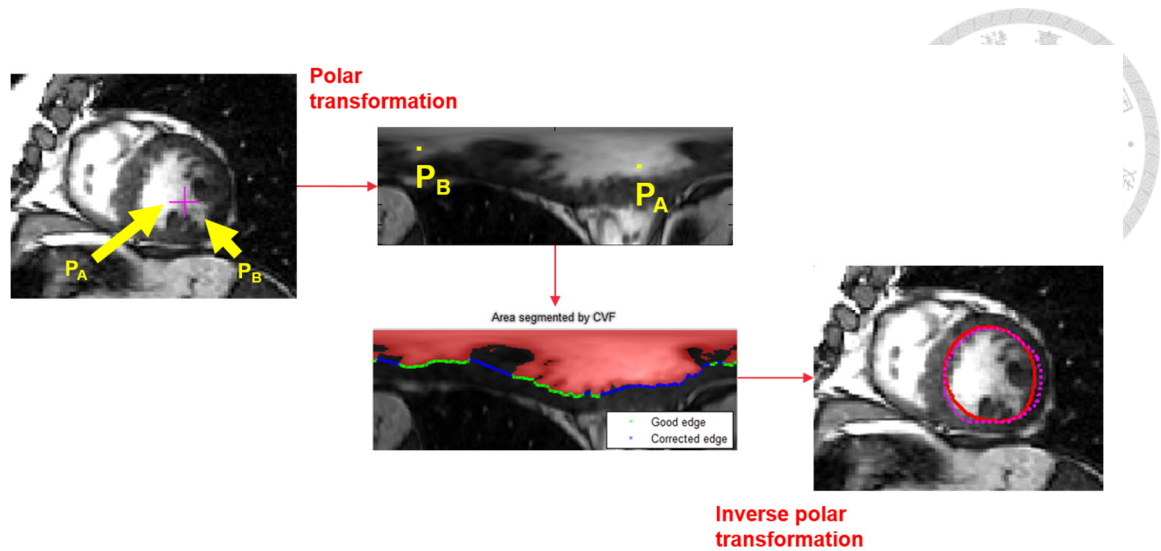
Fig. 4.4   Robustness against field inhomogeneity

The former, the field inhomogeneity, imposes a bias field on the afflicted MR image, resulting in non-uniform signal intensity which is observable on LV blood pool and other tissue types. As a consequence, we should not solely rely on simple histogram-based techniques (including Otsu's thresholding, GMM-based thresholding) to classify the LV blood pool as they completely ignore the spatial relationship of the neighboring pixels (or voxels in the context of CMR volume). In CVF-based segmentation, the image is first transformed into cost volume and the label with least cost is selected after cost within every cost slice is aggregated based on spatial proximity and intensity similarity. Therefore, CVF will return clustered group of labels. Furthermore, CVF acts like a classifier with adaptive threshold. These characteristics makes CVF ideal for combating against field inhomogeneity. See Fig. 4.4 for an example. Point A (P_A) and Point B (P_B) belongs to the region of LV blood pool. Due to field inhomogeneity, they apparently do not have the same signal intensity. What is interesting here is the darkest area in the blood pool is almost the same as the brightest area in the myocardium. Depending on the threshold value chosen, too high, we risk mistakenly label the myocardium as LV blood
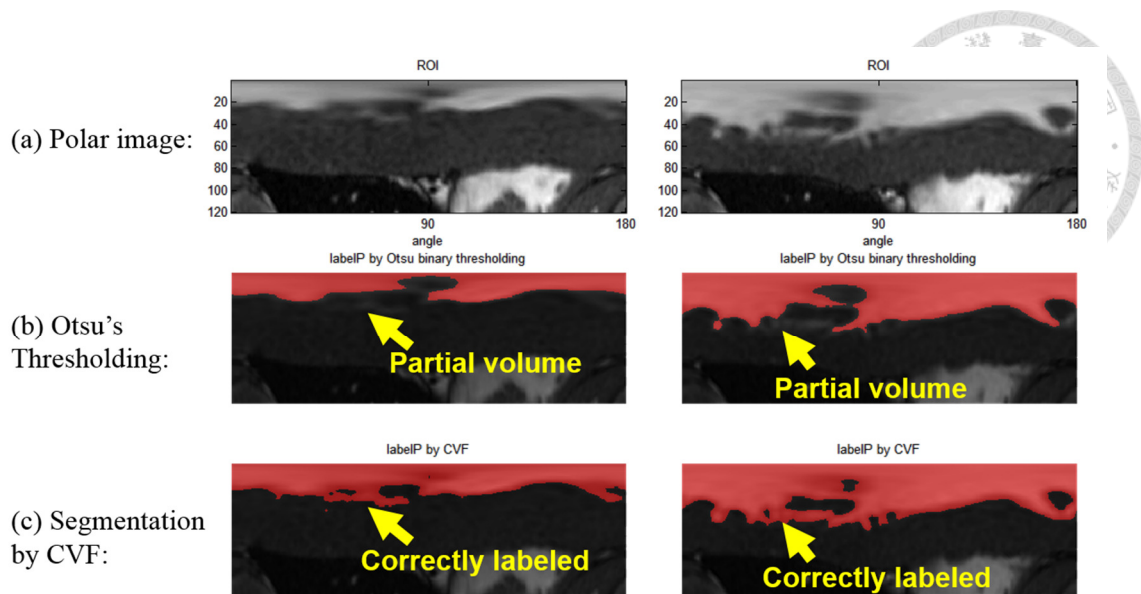
45

Fig. 4.5   Robustness against partial volume effect.

pool. Too low, then not all LV blood pool can be correctly labeled. We may need adaptive threshold for this case. Here, we choose CVF because it is more versatile: it is a general solution for refining multi-label problems. And we can alter the cost for each label in different situations. For example, in hypertrophic cases, we alter the cost so that it is easier to be classified as LV blood pool, and we have found this versatility valuable in the context of CMR image segmentation.

The latter, the partial volume effect, causes the signal of many tissue types to mix up and averaged together if the tissue are in close proximity to each other. Partial volume effect is very common in areas where the papillary muscle and trabeculae carneae are almost collapsed together with the endocardium border. It causes an ambiguity that previous methods are often failed to label correctly. We argue that CVF is effective against partial volume effect. See Fig. 4.5 for examples of two similar cases. In Fig. 4.5(a) shows the original images of the LV after polar transformation. Fig. 4.5(b) and (c) compares the segmentation result from Otsu's thresholding and CVF-based method, respectively. The CVF-based method shows vast improvement over the popular Otsu's method. All the

ambiguities caused by partial volume effect are recovered by the proposed CVF-based segmentation. All these improvements add up. Combined with the proposed endocardial processing framework, the CVF indeed returns results that show major improvements over previous methods.

For additional visual assessment of the proposed method, Fig. 4.6 demonstrates one of our best results from patients stricken by heart failure. Since the endocardium border is clearly defined in both ES and ED phases, the proposed method delineates the endocardium accurately. Fig. 4.7 and Fig. 4.8 show relatively poor performance in the case of hypertrophy. However, delineating endocardium border in hypertrophic hearts is recognized as a very challenging task, as shown in previous findings [11], [12], [17], [34], [37]. Our segmentation result is nevertheless an improvement over previous works.

With little modification to cost volume initialization, we also attempted to apply the method to LV epicardium delineation. However, preliminary result is not favorable. It is at best among the ranks of average performers. And since it is only experimental, we do not publish the exact results here. One reason for the proposed method to fall short on epicardium delineation is the intrinsic limitation of CVF: that CVF relies on intensity similarity to gather costs from corresponding neighbors. Since the signal intensity difference between the myocardium and its neighboring tissues is not as clearly defined as that between the myocardium and blood pool, it is very easy to mislabel the nearby tissues. Given this finding, it might not be suitable to use intensity similarity for epicardium delineation. Gradient-based methods, such as active appearance model or active contour model, could be more promising. It will need more investigation to see whether gradient information can be used in CVF to prevent such mislabel problems.

ES phase

ED phase
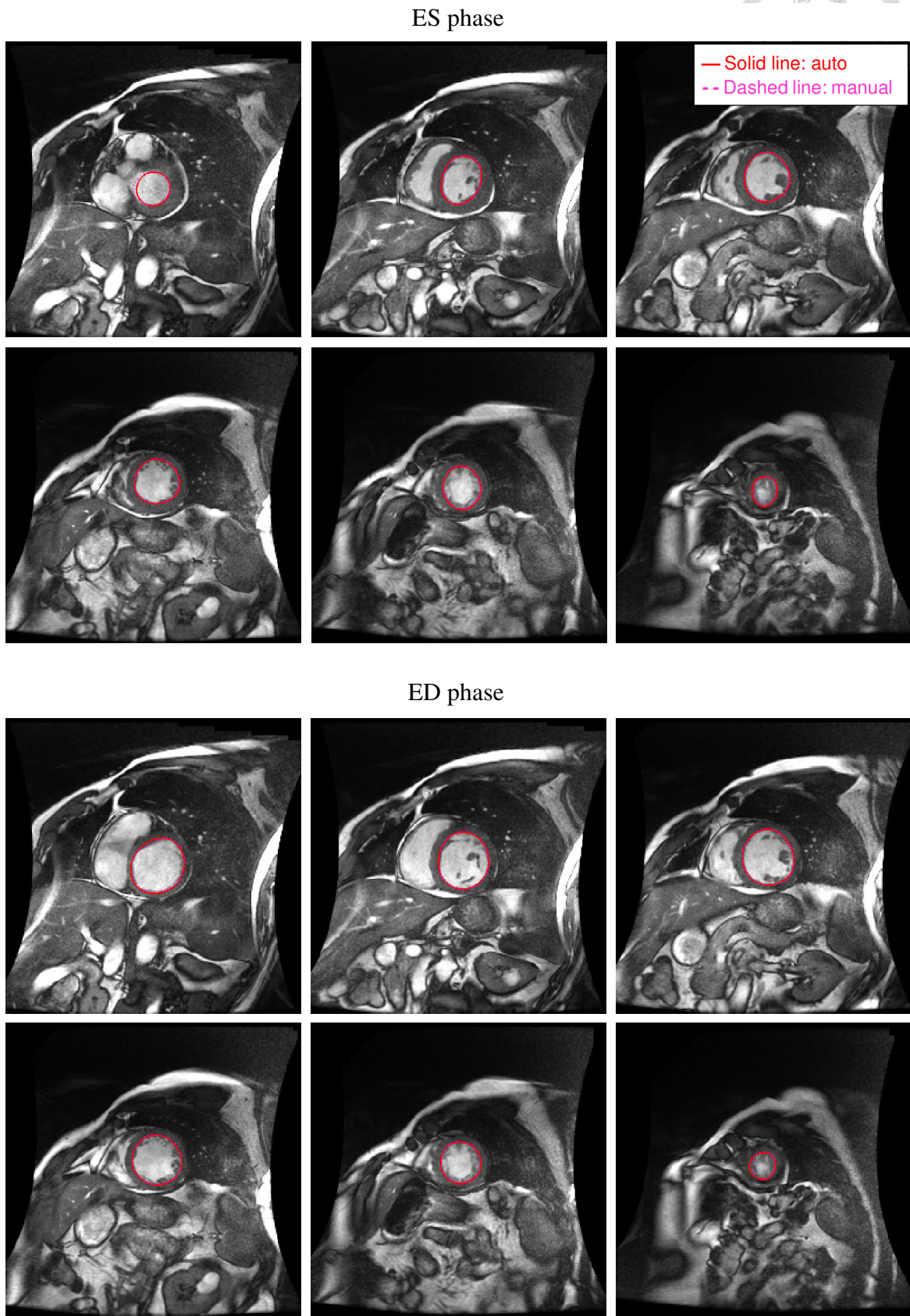
Fig. 4.6   Selected results from patient SC-HF-I-06.

ES phase

— Solid line: auto
- - Dashed line: manual
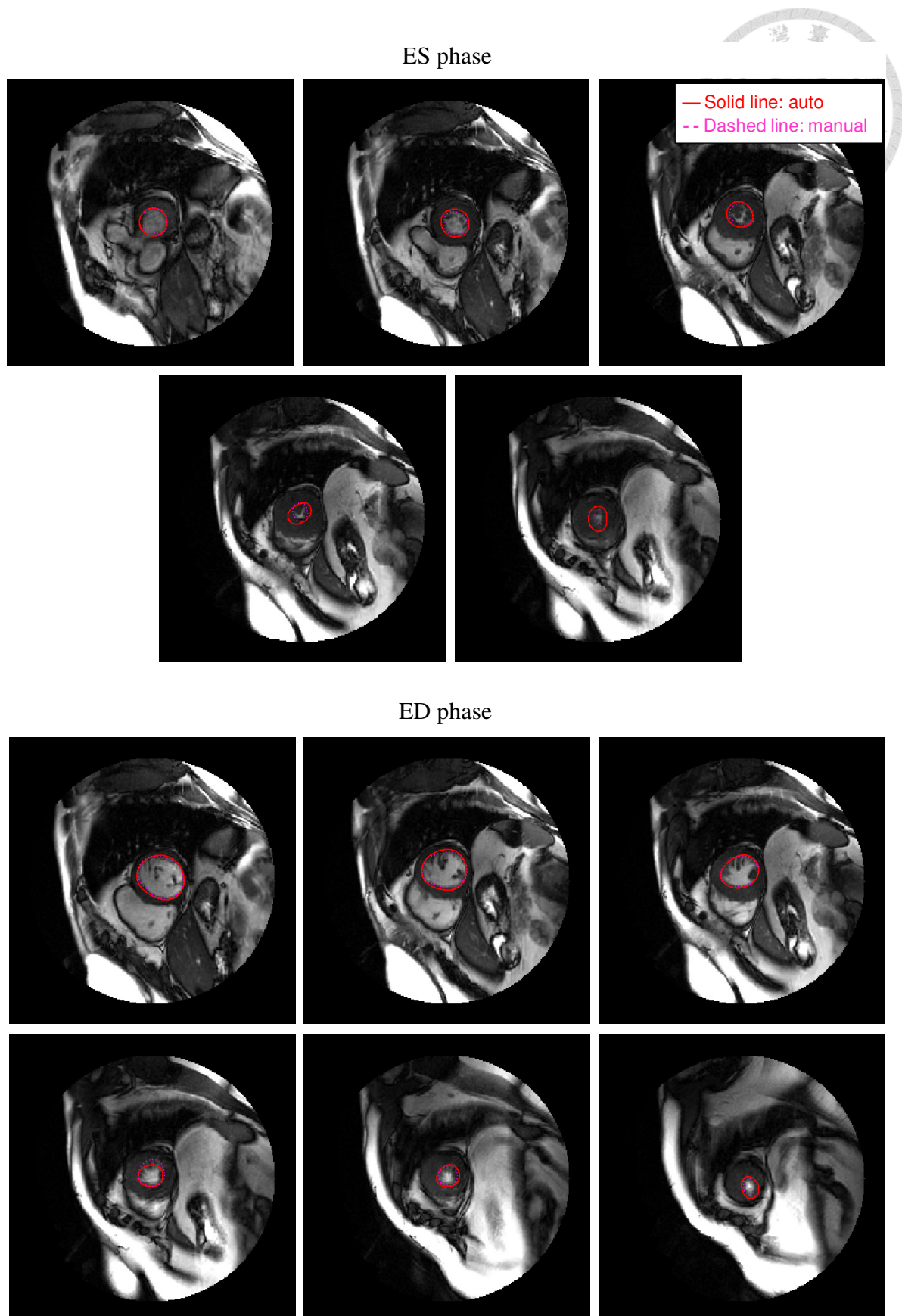
ED phase

Fig. 4.7   Selected results from patient SC-HYP-37. The proposed algorithm still manage to find the endocardium border even when PMTC tissues collapse together.
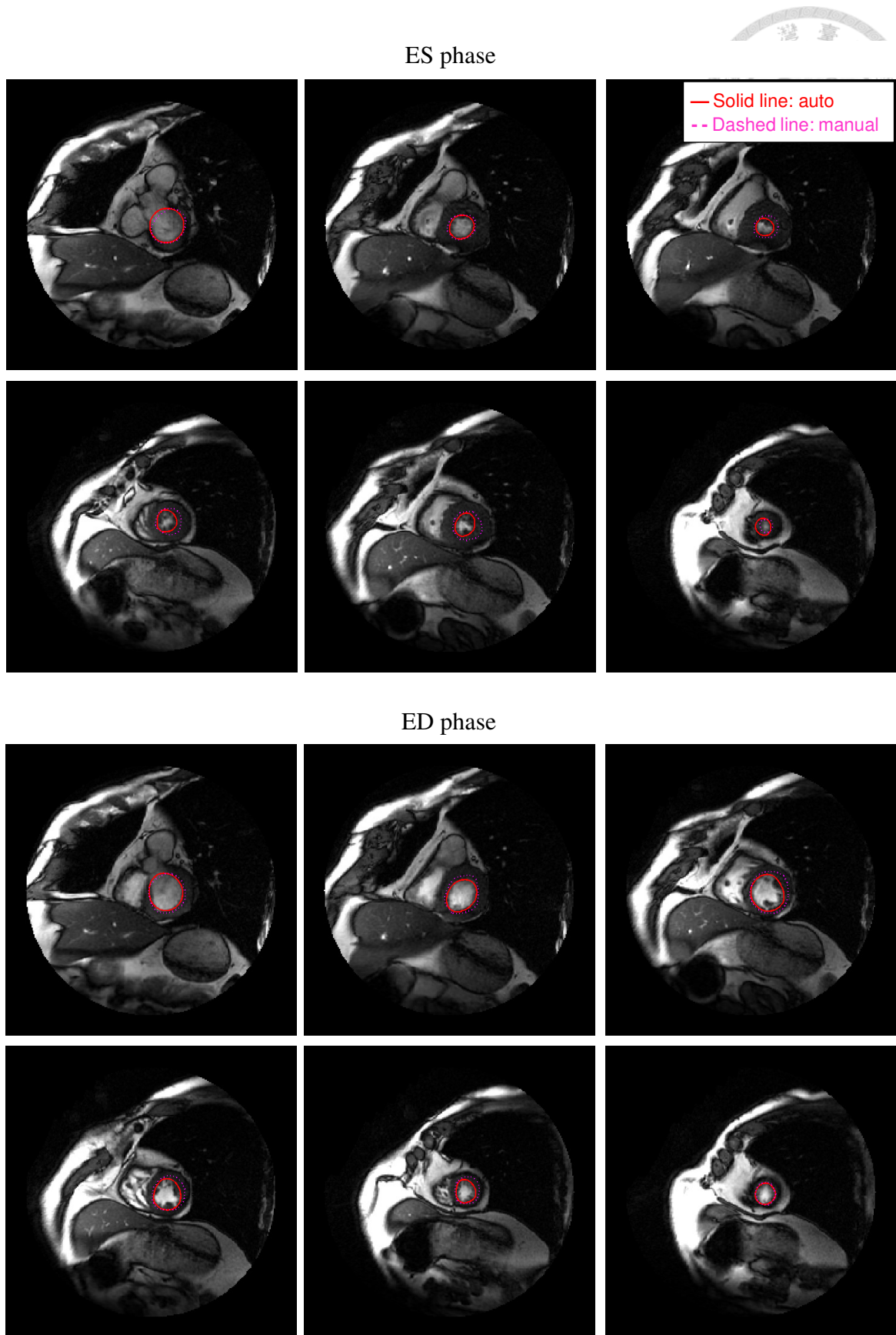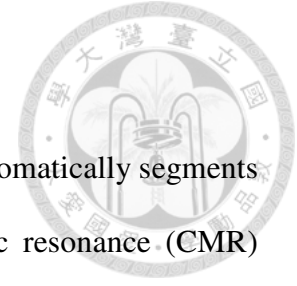
ES phase

ED phase

Fig. 4.8 Selected results from patient SC-HYP-38. The PMTC tissues collapse together and obscure the endocardium border at ES; segmentation error can be observed.

Chapter 5   Conclusion

In this thesis, we have proposed a computational framework that automatically segments the left ventricle in short-axis (SAX) view cine cardiac magnetic resonance (CMR) images. We employ novel cost-volume filtering (CVF) scheme combined with novel myocardial contour processing framework to overcome the segmentation difficulty resulted from PMTC (papillary muscle and trabeculae carneae) tissues that prevents previous methods from achieving high segmentation accuracy. Experimental result shows improved accuracy and robustness over previous works. Highlights regarding this work are:

- The first work to use CVF in the context of medical image segmentation. Furthermore, we have proposed a novel cost initialization scheme specifically tailored to CMR images for improved accuracy.

- The contour processing framework processes the 1D contour function transformed from the segmentation result produced by CVF. By exploiting gradient information, a complimentary contour is also generated. In the final stage, two raw contours obtained from region-based CVF and gradient-based Canny's edge detector undergo a combination and regularization process in which suitable weighting function for each raw contour are determined and additional constraints are enforced.

- One of the issues in previous left ventricle segmentation methods is erroneously including the papillary muscle and trabeculae as a part of the myocardium. A new constraint in contour regularization process is proposed to ensure exclusion of them. To our knowledge, no other works have used similar methods nor do they consider this piece of information to improve myocardial contour accuracy.

- Our method is robust against various pathologies. Specifically, a total of 45 subjects spanning three pathological plus one healthy cases are tested. All four cases show improvement in segmentation accuracy and in derived cardiac parameters.

Furthermore, given that many information are yet to be exploited, such as the inherent 3D information in CMR volume and heart movement constraints, we believe the performance of the proposed segmentation algorithm can be improved much further once all the information is taken into consideration. In addition to the quantitative analysis that shows close correlation between manual and automated segmentation, the high segmentation accuracy and low manual intervention rate suggest our work has potential to accurate 3D reconstruction of left ventricle for visualizing the shape and motion of the left ventricle. Future work includes exploiting inter-slice and inter-time relationships in order to optimize the contour globally, as well as extending this methodology to the delineation of left ventricular epicardial contour, which will make additional clinical parameters such as myocardial mass available.

REFERENCE

[1] Global status report on noncommunicable diseases 2010. Geneva, World Health Organization, 2011.

[2] P. A. Heidenreich, J. G. Trogdon, O. A. Khavjou, J. Butler, K. Dracup, M. D. Ezekowitz, E. A. Finkelstein, Y. Hong, S. C. Johnston, A. Khera, D. M. Lloyd-Jones, S. A. Nelson, G. Nichol, D. Orenstein, P. W. F. Wilson, and Y. J. Woo, "Forecasting the Future of Cardiovascular Disease in the United States A Policy Statement From the American Heart Association," *Circulation*, vol. 123, no. 8, pp. 933–944, Mar. 2011.

[3] K. S. Reddy and S. Yusuf, "Emerging Epidemic of Cardiovascular Disease in Developing Countries," *Circulation*, vol. 97, no. 6, pp. 596–601, Feb. 1998.

[4] H.-Y. Lee, N. C. F. Codella, M. D. Cham, J. W. Weinsaft, and Y. Wang, "Automatic Left Ventricle Segmentation Using Iterative Thresholding and an Active Contour Model With Adaptation on Short-Axis Cardiac MRI," *IEEE Trans. Biomed. Eng.*, vol. 57, no. 4, pp. 905–913, Apr. 2010.

[5] R. J. van der Geest, E. Jansen, V. G. M. Buller, and J. H. C. Reiber, "Automated detection of left ventricular epi- and endocardial contours in short-axis MR images," in *Computers in Cardiology 1994*, 1994, pp. 33–36.

[6] Y.-L. Lu, K. A. Connelly, A. J. Dick, G. A. Wright, and P. E. Radau, "Automatic functional analysis of left ventricle in cardiac cine MRI," *Quant. Imaging Med. Surg.*, vol. 3, no. 4, pp. 200–209, Aug. 2013.

[7] C. Petitjean and J.-N. Dacher, "A review of segmentation methods in short axis cardiac MR images," *Med. Image Anal.*, vol. 15, no. 2, pp. 169–184, Apr. 2011.

[8] C. A. Cocosco, W. J. Niessen, T. Netsch, E. P. A. Vonken, G. Lund, A. Stork, and

M. A. Viergever, "Automatic image-driven segmentation of the ventricles in cardiac cine MRI," *J. Magn. Reson. Imaging*, vol. 28, no. 2, pp. 366–374, Aug. 2008.

[9] S. Xu, C. Pei, and H. Hu, "Endocardium and Epicardium Segmentation in MR Images Based on Developed Otsu and Dynamic Programming," *Sens. Transducers*, Mar. 2014.

[10] S. Huang, J. Liu, L. C. Lee, S. K. Venkatesh, L. L. S. Teo, C. Au, and W. L. Nowinski, "An Image-Based Comprehensive Approach for Automatic Segmentation of Left Ventricle from Cardiac Short Axis Cine MR Images," *J. Digit. Imaging*, vol. 24, no. 4, pp. 598–608, Aug. 2011.

[11] Y. Lu, P. Radau, K. Connelly, A. Dick, and G. Wright, "Automatic Image-Driven Segmentation of Left Ventricle in Cardiac Cine MRI," *MIDAS J. - Card. MR Left Ventricle Segmentation Chall.*, 2009.

[12] S. Huang, J. Liu, L. C. Lee, S. K. Venkatesh, L. L. S. Teo, C. Au, and W. L. Nowinski, "Segmentation of the Left Ventricle from Cine MR Images Using a Comprehensive Approach," *MIDAS J. - Card. MR Left Ventricle Segmentation Chall.*, 2009.

[13] J. Cousty, L. Najman, M. Couprie, S. Clément-Guinaudeau, T. Goissen, and J. Garot, "Segmentation of 4D cardiac MRI: Automated method based on spatio-temporal watershed cuts," *Image Vis. Comput.*, vol. 28, no. 8, pp. 1229–1243, Aug. 2010.

[14] H. Hu, H. Liu, Z. Gao, and L. Huang, "Hybrid segmentation of left ventricle in cardiac MRI using Gaussian-mixture model and region restricted dynamic programming," *Magn. Reson. Imaging*, vol. 31, no. 4, pp. 575–584, May 2013.

[15] Nobuyuki Otsu, "A Threshold Selection Method from Gray-Level Histograms," *IEEE Trans. Syst. Man Cybern.*, vol. 9, no. 1, pp. 62–66, Jan. 1979.

[16] C. Constantinides, E. Roullot, M. Lefort, and F. Frouin, "Fully automated

segmentation of the left ventricle applied to cine MR images: Description and results on a database of 45 Subjects," in *2012 Annual International Conference of the IEEE Engineering in Medicine and Biology Society (EMBC)*, 2012, pp. 3207–3210.

[17] J. Wijnhout, D. Hendriksen, H. Van Assen, and R. Van der Geest, "LV Challenge LKEB Contribution: Fully Automated Myocardial Contour Detection," *MIDAS J. - Card. MR Left Ventricle Segmentation Chall.*, 2009.

[18] I. Ben Ayed, S. Li, and I. Ross, "Embedding Overlap Priors in Variational Left Ventricle Tracking," *IEEE Trans. Med. Imaging*, vol. 28, no. 12, pp. 1902–1913, Dec. 2009.

[19] G. Tarroni, D. Marsili, F. Veronesi, C. Corsi, C. Lamberti, and G. Sanguinetti, "Near-automated 3D segmentation of left and right ventricles on magnetic resonance images," in *2013 8th International Symposium on Image and Signal Processing and Analysis (ISPA)*, 2013, pp. 522–527.

[20] M. Lynch, O. Ghita, and P. F. Whelan, "Segmentation of the Left Ventricle of the Heart in 3-D+t MRI Data Using an Optimized Nonrigid Temporal Model," *IEEE Trans. Med. Imaging*, vol. 27, no. 2, pp. 195–203, Feb. 2008.

[21] Q. C. Pham, F. Vincent, P. Clarysse, P. Croisille, and I. E. Magnin, "A FEM-based deformable model for the 3D segmentation and tracking of the heart in cardiac MRI," in *Proceedings of the 2nd International Symposium on Image and Signal Processing and Analysis, 2001. ISPA 2001*, 2001, pp. 250–254.

[22] J. Schaerer, C. Casta, J. Pousin, and P. Clarysse, "A dynamic elastic model for segmentation and tracking of the heart in MR image sequences," *Med. Image Anal.*, vol. 14, no. 6, pp. 738–749, Dec. 2010.

[23] C. Casta, P. Clarysse, J. Schaerer, and J. Pousin, "Evaluation of the Dynamic Deformable Elastic Template model for the segmentation of the heart in MRI sequences,"

MIDAS J. - Card. MR Left Ventricle Segmentation Chall., 2009.

[24] M.-P. Jolly, C. Guetter, X. Lu, H. Xue, and J. Guehring, "Automatic Segmentation of the Myocardium in Cine MR Images Using Deformable Registration," in *Statistical Atlases and Computational Models of the Heart. Imaging and Modelling Challenges*, O. Camara, E. Konukoglu, M. Pop, K. Rhode, M. Sermesant, and A. Young, Eds. Springer Berlin Heidelberg, 2012, pp. 98–108.

[25] M. Lorenzo-Valdés, G. I. Sanchez-Ortiz, A. G. Elkington, R. H. Mohiaddin, and D. Rueckert, "Segmentation of 4D cardiac MR images using a probabilistic atlas and the EM algorithm," *Med. Image Anal.*, vol. 8, no. 3, pp. 255–265, Sep. 2004.

[26] V. Hartwig, G. Giovannetti, N. Vanello, M. Lombardi, L. Landini, and S. Simi, "Biological effects and safety in magnetic resonance imaging: a review," *Int. J. Environ. Res. Public. Health*, vol. 6, no. 6, pp. 1778–1798, Jun. 2009.

[27] A. O. Zurick, J. L. Klein, and M. S. Runge, *Netter's Cardiology*, 2nd ed. Elsevier, 2010.

[28] M.-P. Jolly, "Automatic Recovery of the Left Ventricular Blood Pool in Cardiac Cine MR Images," in *Medical Image Computing and Computer-Assisted Intervention – MICCAI 2008*, D. Metaxas, L. Axel, G. Fichtinger, and G. Székely, Eds. Springer Berlin Heidelberg, 2008, pp. 110–118.

[29] C. Rhemann, A. Hosni, M. Bleyer, C. Rother, and M. Gelautz, "Fast cost-volume filtering for visual correspondence and beyond," in *2011 IEEE Conference on Computer Vision and Pattern Recognition (CVPR)*, 2011, pp. 3017–3024.

[30] A. Pednekar, U. Kurkure, R. Muthupillai, S. Flamm, and I. Kakadiaris, "Automated left ventricular segmentation in cardiac MRI," *IEEE Trans. Biomed. Eng.*, vol. 53, no. 7, pp. 1425–1428, Jul. 2006.

[31] K. He, J. Sun, and X. Tang, "Guided Image Filtering," *IEEE Trans. Pattern Anal.*

Mach. Intell., vol. 35, no. 6, pp. 1397–1409, Jun. 2013.

[32] J. Canny, "A Computational Approach to Edge Detection," *IEEE Trans. Pattern Anal. Mach. Intell.*, vol. PAMI-8, no. 6, pp. 679–698, Nov. 1986.

[33] P. Radau, Y. Lu, K. Connelly, G. Paul, A. J. Dick, and G. A. Wright, "Evaluation Framework for Algorithms Segmenting Short Axis Cardiac MRI.," *MIDAS J. - Card. MR Left Ventricle Segmentation Chall.*, 2009.

[34] M. Jolly, "Fully automatic left ventricle segmentation in cardiac cine MR images using registration and minimum surfaces," *MIDAS J.-Card. MR Left Ventricle Segmentation Chall.*, vol. 4, 2009.

[35] C. Feng, C. Li, D. Zhao, C. Davatzikos, and H. Litt, "Segmentation of the Left Ventricle Using Distance Regularized Two-Layer Level Set Approach," in *Medical Image Computing and Computer-Assisted Intervention – MICCAI 2013*, K. Mori, I. Sakuma, Y. Sato, C. Barillot, and N. Navab, Eds. Springer Berlin Heidelberg, 2013, pp. 477–484.

[36] T. A. Ngo and G. Carneiro, "Left ventricle segmentation from cardiac MRI combining level set methods with deep belief networks," in *2013 20th IEEE International Conference on Image Processing (ICIP)*, 2013, pp. 695–699.

[37] C. Constantinides, Y. Chenoune, N. Kachenoura, E. Roullot, E. Mousseaux, A. Herment, and F. Frouin, "Semi-automated cardiac segmentation on cine magnetic resonance images using GVF-Snake deformable models," *MIDAS J. - Card. MR Left Ventricle Segmentation Chall.*, 2009.

[38] L. Cordero-Grande, G. Vegas-Sánchez-Ferrero, P. Casaseca-de-la-Higuera, J. Alberto San-Román-Calvar, A. Revilla-Orodea, M. Martín-Fernández, and C. Alberola-López, "Unsupervised 4D myocardium segmentation with a Markov Random Field based deformable model," *Med. Image Anal.*, vol. 15, no. 3, pp. 283–301, Jun. 2011.